Processing, characterization and *in-vitro* biodegradation of AE42 magnesium alloy coated with silane-PMMA for cardiovascular stent application

A THESIS SUBMITTED FOR THE

PARTIAL FULFILLMENT OF THE REQUIREMENT FOR THE DEGREE OF

Master of Technology

in

Biomedical Engineering

by

OMKAR MAJUMDER

213BM1009

UNDER THE SUPERVISION OF

Dr. A. THIRUGNANAM

DEPARTMENT OF BIOTECHNOLOGY AND MEDICAL ENGINEERING

NATIONAL INSTITUTE OF TECHNOLOGY ROURKELA

ROURKELA, ODISHA, INDIA-769008

MAY 2015

Department of Biotechnology and Medical Engineering

National Institute of Technology Rourkela, Odisha, India-769008

CERTIFICATE

This is to certify that the thesis entitled **"Processing, characterization and *in-vitro* biodegradation of AE42 magnesium alloy coated with silane-PMMA for cardiovascular stent application"** is a record of the bonafide work done by OMKAR MAJUMDER (213BM1009) which is submitted for partial fulfilment of the requirements for the degree of Master of Technology (M.Tech) in Biomedical Engineering at National Institute of Technology, Rourkela. To the best of my knowledge, the matter embodied in the thesis has not been submitted to any other University/Institute for the award of any Degree or Diploma.

Place: NIT Rourkela
Date: 01 June, 2015

Dr. A. Thirugnanam (Supervisor)
Assistant Professor
Biotechnology and Medical Engineering
National Institute of Technology
Rourkela-769 008, Odisha (India)

Acknowledgement

Successful completion of this project is the outcome of consistent guidance and assistance from many people, faculty and friends and I am extremely fortunate to have got these all along the completion of the project.

I owe my profound gratitude and respect to my project supervisor, Dr. A. Thirugnanam, Department of Biotechnology and Medical Engineering, NIT Rourkela for his invaluable academic support and professional guidance, regular encouragement and motivation at various stages of this project. I am deeply grateful to Dr. A. K. Mondal, Department of Metallurgical and Materials Engineering, NIT Rourkela whose insights and ideas have contributed so much to this thesis. I place on record my sincere gratitude to Prof. Krishna Pramanik, Head of Department, Department of Biotechnology and Medical Engineering, NIT Rourkela for her constant encouragement.

I would like to thank Mr. Chandra Shekhar Perugu, Department of Materials Engineering, Indian Institute of Science Bangalore, Ms. Tejinder Kaur, Ms. Reshmi Dey, Mr. Sumanta Kar, Mr. Basil Mathai, Ms. Veena Vyas, Mr. K. Senthil Guru Department of Biotechnology and Medical Engineering, Mr. A.K.S. Bankoti, Ms. Shreya Mukherjee, Mr. Pranav Bhale, Mr. Hrishikesh Shastri, Department of Metallurgical and Materials Engineering, Mr. Rahul Kumar Malik, Department of Electronics and Communication Engineering, Mr. Snehasis Biswas, Mr. Ranajit Mondal, Department of Chemical Engineering, Mr. Rakesh Muduli and Mr. Ranjit Panda, Department of Physics, NIT Rourkela for their regular support, help and motivation.

I would also thank my institution and my faculty members without whom this project would have been a distant reality. I also extend my thanks to my parents and well-wishers.

Place: NIT Rourkela **Omkar Majumder**

Date: 01 June, 2015 **(213BM1009)**

I dedicate this project to

my motherland

ABSTRACT

In the present study, AE42 Mg alloy was squeeze-cast and its microstructural analysis was performed using optical and field emission scanning electron microscope (FESEM). The casted AE42 Mg alloy was alkali pre-treated (NaOH 3M, for 10 days) before coating. The alkali pre-treated specimen was coated with silane and silane-polymethylmethacrylate (PMMA) by sol-gel technique. The coatings were characterized using FESEM, energy dispersive spectroscopy (EDS) and Fourier transform infrared (FTIR) spectroscopy. The adhesion strength and the hardness of the coatings on the substrates were evaluated using ASTM standards. The *in-vitro* biodegradation of the uncoated and coated specimens in simulated body fluid (SBF) were studied under static and dynamic conditions for 7 days. The variation in pH and the ionic concentrations of the SBF were measured during this period. The corrosion resistance of coated and uncoated specimens were investigated in SBF using hydrogen evolution, potentiodynamic polarization and electrochemical impedance spectroscopy (EIS) analyses. In addition, contact angle, protein adsorption and hemocompatibility of all the specimens were also studied to establish its significance for cardiovascular stent application. The results confirmed that the silane-PMMA coating showed less *in-vitro* biodegradation with improved corrosion resistance and also enhanced hemocompatibility of the material making it favourable candidate for biodegradable stent applications.

Keywords: AE42 Mg alloy, silane-PMMA coating, corrosion resistance, biodegradable stent.

CONTENTS

Page No.

LIST OF FIGURES

LIST OF TABLES

LIST OF ABBREVIATIONS

APTES	*3-(aminopropyl)triethoxysilane*
CPE	Constant phase element
EDS	Electron dispersive spectroscopy
EIS	Electrochemical impedance spectroscopy
FTIR	Fourier transformed infrared spectroscopy
HR	Hemolysis ratio
PMMA	*Polymethylmethacrylate*
SBF	Simulated body fluid
S-Coated	Silane coated
SEM	Scanning electron microscope
SP-Coated	Silane-PMMA coated
XRD	X-ray diffraction

CHAPTER 1

INTRODUCTION

In recent years, there is great upsurge of using biodegradable materials for advanced implants and tissue scaffolds. These biodegradable materials should be able to stimulate the healing responses of injured tissues in the physiological environment. For example, the stents made of conventional non-degradable metals and polymers, might negatively interact with the surrounding tissues and results in long-term endothelial dysfunction, delayed re-endothelialization, late thrombosis, permanent physical irritation, toxic metal ion release, local chronic inflammation and so on [1]. Thus, the materials exhibiting biodegradability are preferred over the stable and inert ones as in most cases body requires only the temporary presence of an implant. The biodegradable implanted stents are degraded or absorbed after they fulfill the desired objectives and eliminates the requirement of follow-up surgery to remove them.

In the past decade, pure magnesium (Mg) and its alloys received considerable attention over polymers as promising candidates for new generation stent materials for human body owing to their excellent *in-vivo* biodegradability, appropriate mechanical properties, and favorable

compatibility in the physiological environment [2]. Accordingly, Mg alloys were investigated extensively as biodegradable implants for the application of bone fixation devices, cardiovascular stents and tissue engineering scaffolds. Mg-rare earth (RE) based alloys are reported to exhibit the highest strength and ductility, the best corrosion resistance and great biosafety in the form of both stents and screws [3]. Mg is an electrochemically active metal and very prone to corrosion owing to its position in the electromotive force (EMF) series. Therefore, the major challenge of using Mg and its alloys as temporary implants for biomedical application is to control their high corrosion rate. Corrosion is too rapid even for a biodegradable material and, additionally, it is not homogeneous, due to a strong tendency for localized corrosion exhibited by Mg alloys. In addition, there is a tendency of formation of hydrogen bubbles (also known as balloon effect) by corrosion reaction owing to the very rapid evolution of hydrogen that body cannot absorb [4]. It also hinders cell bonding to the implant surface. Additionally, a shift in pH towards alkaline in the vicinity of the corroded surface is also of concern for medical applications.

Several attempts were made to increase the corrosion resistance of Mg alloys by modifying them [4]. However, the modification by alloying additions is limited owing to the low solubility of elements in Mg, and therefore, the application of coatings is regarded as one of the most promising method to improve corrosion resistance. For biomedical applications, besides corrosion protection, the coatings should also possess other functions, such as enhancement of biocompatibility, bioactivity, antibiotic ability or local drug delivery ability. Moreover, the specific coatings should enable biodegradation at a desired rate, and hence should offer only a limited barrier function. Such coatings should be nontoxic and their breakdown products should be biodegradable as well. Surface modifications based on silane coating were very attractive in enhancing the corrosion resistance of metallic substrates. These coatings are environment friendly, their application processes are uncomplicated, and so, they are increasingly attractive to improve the corrosion resistance of a wide range of metals and alloys. Silane coated surfaces have also been found to be biocompatible and have been widely used for biological interactions, protein absorption, cellular and bacterial adhesion [5-8].

In the present investigation, AE42 alloy was squeeze-cast and a silane coating of 3-aminopropyltriethoxysilane (APTES) and silane-polymethylmethacrylate (PMMA) coating

were deposited on the alkali pretreated alloy specimens by sol-gel process. The characteristics of the coatings and corrosion resistance in simulated body fluid (SBF) were systematically investigated using field emission scanning electron microscope (FESEM), Fourier transform infrared (FTIR) spectroscopy, pH study, hydrogen evolution, potentiodynamic polarization, electrochemical impedance spectroscopy (EIS) and X-ray diffraction (XRD) analyses. The degradation performance and mechanism were also discussed.

CHAPTER 2

LITERATURE REVIEW

Mg is a lightweight metal that has low density and good mechanical properties. Some of the properties of Mg such as its elastic modulus, density and yield strength are very close to natural bone when compared to other implants, resulting in reduction of stress shielding and better bone formation. A comparison of the mechanical properties of Mg and various implant materials with respect to natural bone are shown in Table 2.1 [7].

However, the main limitation of Mg alloys as medical implants is their high rate of corrosion. Corrosion occurs too rapidly even for a biodegradable material that finally leads to the poor mechanical performance of these alloys. The types of corrosion that affects Mg alloys can be classified as:

2.1 Types of Corrosion

2.1.1 Galvanic corrosion

Mg is highly reactive owing to its lower position in the EMF series. Hence, the metallic phases that are found Mg alloys, increase the chances of internal galvanic attack [8]. This kind of galvanic attack leads to severe localized corrosion to the anodic phase adjacent to the

secondary cathodic phase [9]. Song et al. [10] observed some large pits next to the cathodic second phase in a Mg-Zn-Y-Zr wrought alloy that was due to the galvanic corrosion induced by the secondary phase. Cathodes can be classified as external and internal cathodes. External cathodes are those metals that are in contact with Mg externally whereas the internal cathodes are the secondary phases and the impurities present in the alloy [9].

Table 2.1 The mechanical properties of various implant materials.

	Density (g/cm^3)	**Elastic modulus (GPa)**	**Compressive yield strength (MPa)**	**Fracture toughness ($MPam^{1/2}$)**
Natural Bone	1.8-2.1	3-20	130-180	3-6
Magnesium	1.74-2.0	41-45	65-100	15-40
Ti alloy	4.4-4.5	110-117	758-1117	55-115
Co-Cr	8.3-9.2	230	450-1000	N/A
Stainless Steel	7.9-8.1	189-205	170-310	50-200
Synthetic hydroxyapatite	3.1	73-117	600	0.7

2.1.2 Pitting corrosion

The surface heterogeneity that exists due to presence of secondary phases and the passivation layer breakdown on the alloy surface leads to pitting corrosion in metals. Zeng et al. observed corrosion pits in Mg alloys adjacent to the secondary phases such as $Al_{12}Mg_{17}$ and AlMn, due to the local breakdown of the passivation layer and thereby, formation of an electrolytic cell in between the cathodic second phases and the anodic Mg matrix [11].

2.1.3 Intergranular corrosion

Intergranular corrosion does not take place in Mg alloys. This is due to the fact that the secondary β phase precipitated along the grain boundaries become cathodic to the α-Mg matrix. Aung et al. observed intragranular corrosion within the α-Mg grains in the AZ31B-H24 Mg alloy. The presence of the twins and Al–Mn–Fe phases in the alloy acted as cathode and thus, lead to anodic corrosion of the α-Mg grains [12].

2.1.4 Filiform corrosion

This form of corrosion generally occurs under protective coatings. But Ghali et al. [13] observed this form of corrosion with an uncoated AZ31 alloy. It was also observed in uncoated AZ91 to some extent [14].

2.1.5 Stress corrosion cracking (SCC)

Stress corrosion cracking (SCC) occurs when tensile loading as well as corrosive environments combine together and result in cracking of materials. Mg alloys are highly susceptible to SCC in environments containing Cl^- ions [15 - 17]. Orthopedic implants such as pins and screws are affected by tensile and compressive stresses in the body [17]. Also the cardiovascular implants are impacted by the shear stress due to the blood flow [18,19]. Choudhary et al. found brittle cracks associated with SCC stem from corrosion pits, sharp contours and micro-cracks [20].

In general there are two possible ways to improve the corrosion behavior of Mg and Mg alloys [4]:

(i) tailoring the microstructure and composition, including the texture and grain size of the base material, not only through alloying but also through the development of optimized manufacturing methods [12, 21, 22];

(ii) surface treatments or form coatings, which can effectively produce protective ceramic, polymer or composite layers [1, 5, 23-32].

2.2 Coatings on Mg and Mg alloys

2.2.1 Sol-gel coatings

Forming inorganic biodegradable coatings on Mg alloys by dip coating without reactions with the substrate is rare. There have been several studies of sol-gel based coatings that also include subsequent heat treatment steps, required to further intensify the ceramic layer for better corrosion resistivity. Feil et al. [25] successfully implemented SiO_2 layers on Mg alloy AZ31 from sols via dipping and also via electrophoretic deposition (EPD). Shi et al. [26] showed the improvement in corrosion resistance by fixing TiO_2 sol on pure Mg. The coating process was repeated several times to obtain a proper coating and the TiO_2 phase was found to be amorphous. Thick porous calcium phosphate and Si-containing calcium phosphate coatings were synthesized and coated via sol-gel method by Roy et al. [27]. Higher concentrations of HA were reported on the layers containing Si. *In-vitro* biodegradation tests in Dulbecco's modified Eagle's medium (DMEM) showed that the coating layers were stable for at least 3 days. The porosity and the cracks present in those films made them incapable of reducing the rate of degradation of the substrate. However, cell tests showed that the coated substrates were more cytocompatible than the uncoated Mg alloy. Gaur et al. [5] also developed a silane based composite biodegradable coating consisting of variant ratios of diethylphosphatoethyltriethoxysilane (DEPETES) and bis-[3-(triethoxysilyl) propyl] tetrasulfide (BTESPT) via sol-gel route. This coating improved the corrosion resistivity as well as the biocompatibility in m-SBF.

2.2.2 Dip coatings of organic polymers

Dip coating to acquire natural biopolymer coatings on Mg and Mg alloy substrates has got wider consideration than dip coating of inorganic coatings. Li et al. [28], for instance, created a polylactic-co-glycolic corrosive (PLGA) coating on Mg6Zn substrates. The coating thickness (33 and 72 µm) was controlled by the PLGA concentration. Corrosion tests utilizing polarization and impedance tests performed in NaCl arrangement exhibited a lower degradation rate because of the biopolymer coating. Voids and defects in the thick coating (72 µm) caused lower corrosion resistance than the thin coating of 33 µm. Also the PLGA coating affected the cell culture tests with MC3T3-E1 osteoblast cells on the thin coatings with better

cell adhesion. Chen et al. [24] effectively synthesized polycaprolactone (PCL) and polylactic acid (PLA) coatings with thicknesses of around 15-20 μm on pure Mg surfaces. Conventional potentiodynamic polarization tests and corrosion tests under dynamic conditions were performed in SBF to reproduce stent environment. Other than some resistance to corrosion due to the presence of the coatings, dynamic degradation tests showed a particular interaction between the substrate and polymer coating which undermined the corrosion resistance. This study also proposed that this sort of interaction might happen for Mg stents coated with biodegradable polymers, which could be a major challenge for the further improvement of Mg based stents.

CHAPTER 3

MATERIALS AND METHODS

3.1 Materials

3.1.1 Mg alloy casting

Direct squeeze-casting technique was employed to fabricate the AE42 Mg alloy. The alloy was first melted at 770°C and it was then poured in a preheated die manually. The upper arm of a vertical hydraulic press squeezed the melt with a speed of 10 mm/s.

Table 3.1 Chemical composition of the AE42 alloy.

Element	**Mg**	**Al**	**Ce**	**La**	**Nd**	**Mn**	**Fe**
Wt. %	93.6	3.8	1.1	0.7	0.4	0.2	<0.001

The casted part was solidified in 20 s under an applied pressure of 100 MPa. The chemical composition of the alloy is shown in Table 3.1.

3.1.2 Precautions to be taken for casting Mg alloy

A bottom pour type stir squeeze casting machine (SWAMEQUIP, India) is shown in Fig. 3.1. Proper precautions for casting Mg alloy are very essential and the whole process should be handled very carefully. The essential precautionary are:

a. Full mask and safety goggles for the danger of hot metal spilling on the face.

b. Hand gloves for thermal insulation.

c. Closed toe boots.

d. Emergency buckets with sand and CO_2 fire extinguisher for any kind of fire hazard.

e. Alloying elements should be cured and dried properly before adding.

f. Minimum exposure of molten Mg to natural air should be ensured due to chances of rapid oxidation.

3.1.3 Machining of the AE42 specimens

The as-cast alloy was cut for further use in various experiments. This was done by several steps of machining that included the cutting, grinding and lathe cutting and drilling. A cylindrical specimen was finally obtained that was in ready form for further use in the *in-vitro* biodegradation. A brief illustration of the machining process is shown in Fig. 3.2.

3.2 Coating procedure

The AE42 casted alloy was coated with silane (S-coated) as well as silane combined with PMMA (SP-coated). For coating, specimens of 20 mm x 20mm were cut from the castings and its surfaces were polished using SiC papers (up to 1500 grit) and ultrasonicated with deionized water and acetone. The ultrasonicated specimens were immersed in a 3 M NaOH solution of pH 12 maintained at 30°C using a water bath in order to obtain a uniform hydroxide layer on the specimen surfaces before silane adhesion. This was done to improve the silane-substrate bonding. The alkali treated specimens were rinsed with deionized water and acetone, and then dried in hot air. For hydrolysis of ethoxy groups in APTES (Aldrich,

99% pure), 2.21 g of APTES and 18 g of H_2O were mixed and stirred at ambient temperature (~25ºC) for 24 h. Concentrated H_2SO_4 of 0.98 g was added drop wise into the mixture and stirred for 24 h. The obtained solution is denoted as Si-solution [29]. The specimens were immersed into the silane solution for 15 min and dried in air. This coating was cured by heating at 120°C for 1 h in an oven.

The PMMA solution was prepared by dissolving 2 wt. % of PMMA (HiMedia, India) in acetone. The silanized alloy specimens were held vertically and immersed in PMMA solution for 1 h. The dipped specimens were dried in air for 20 min and then cured in an oven at 100°C for 1 h.

Fig. 3.1. A bottom pour type stir squeeze cast machine for casting Mg and Mg alloys.

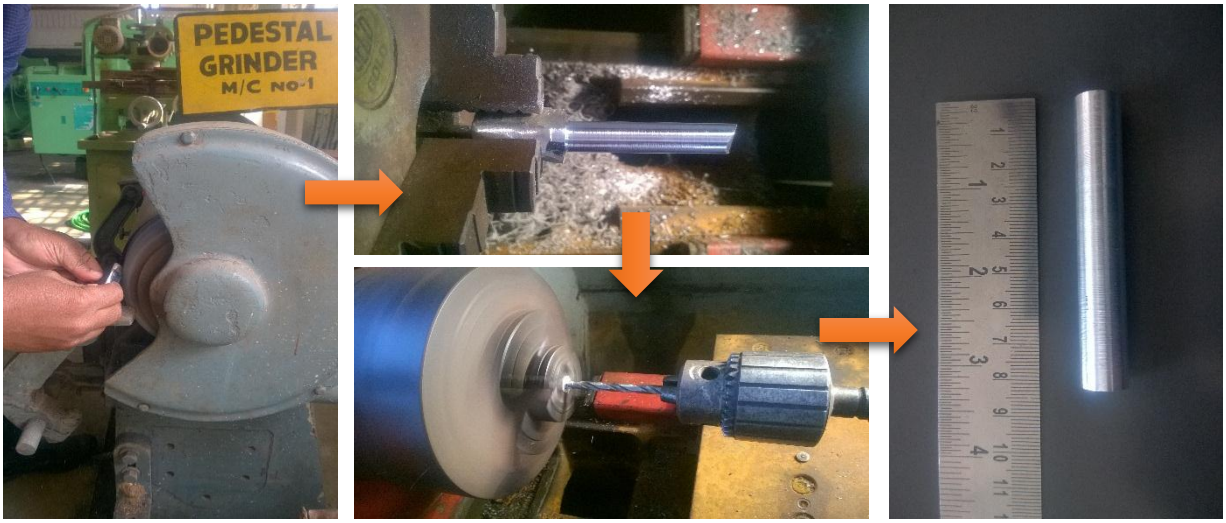

Fig. 3.2. Showing the machining process of the AE42 alloy for use in experiments.

3.3 Characterization

3.3.1 X-ray diffraction

X-ray diffraction (XRD) (Rigaku Ultima-IV) studies were carried out to determine the phases present in the as-cast specimen using CuKα radiation. The scan range (2θ) was from 20-80°. The scan speed was 5°/min and a step size of 0.05 was maintained.

3.3.2 Scanning electron microscopy

The uncoated and coated specimens were characterized using scanning electron microscopy (FEI, FESEM Nova NanoSEM 450) to study the surface morphology and the cross-section of the coatings. Prior to SEM observation, all the specimens were gold sputter coated.

3.3.3 Mechanical characterization

The adhesion of the coatings was determined by tape test in accordance with ASTM D 3359-09 standard [30]. The coated specimen surfaces were cut using a scalpel with a cutting angle in between 15-30° and a pressure sensitive tape was applied and removed rapidly. The pencil hardness of the coatings was determined in accordance with ASTM D 3363-00 standard [31]. Wood pencils of different hardness were procured and scratched on the coated surfaces at an angle of approximately 45° at ambient temperature.

3.3.4 Fourier transform infrared spectroscopy

Fourier transform infrared (FTIR) spectra (Perkin Elmer, RX-I FTIR) was performed on all the coated specimens to study molecular interactions at the coatings. FTIR spectra was done between 4000-500 cm^{-1}.

3.4 Measurement of surface wettability

The surface wettability of the coated and uncoated specimens was measured using a drop size analyzer (DSA 25, KRÜSS GmbH) using double distilled water at ambient temperature. The contact angle measurements were carried out using sessile drop technique. The liquid of 10 µl droplet was allowed to fall on the surface of the specimen, and immediately image of the droplet was captured after 5 s of stabilization. The profile of the droplet was then automatically fitted and the contact angle was measured using DSA 4 software. Six specimens were tested for each condition.

3.5 *In-vitro* biodegradation test

The *in-vitro* biodegradation behavior of the coated and uncoated specimens were evaluated at static immersion (SI) and dynamic flow (DF) conditions. The degradation (SI & DF) was assessed in simulated body fluid (SBF) which was prepared as per Kokubo's protocol [32]. For SI test, the specimens were immersed up to 168 h in SBF maintained at 37±0.5°C using a constant temperature water bath. The concentration of Mg^{2+} in the SBF solution was measured by atomic absorption spectroscopy (Perkin Elmer, AAnalyst 200) at the end of 24, 72, 120 and 168 h. For DF test, a test platform consisting of an electronic controller to monitor the flow rate was designed to simulate the environment experienced by the stents in coronary arteries (Fig. 3.3). A polyurethane tube with an inner diameter of 6 mm was used as channel for the circulating the solution. The specimen having geometry of a circular tube was tightly locked by the pressure exerted on its outer wall by the enlarged tube. The pressure was enough to prevent penetration of solution in between the inner wall of the tube and the outer wall of the specimen. A constant flow was maintained inside the specimen during the test period of 168 h. The pH values of the solution were measured after 1, 2, 4, 6, 8, 10, 12, 24, 48, 72, 96, 120, 144 and 168 h for both SI and DF tests.

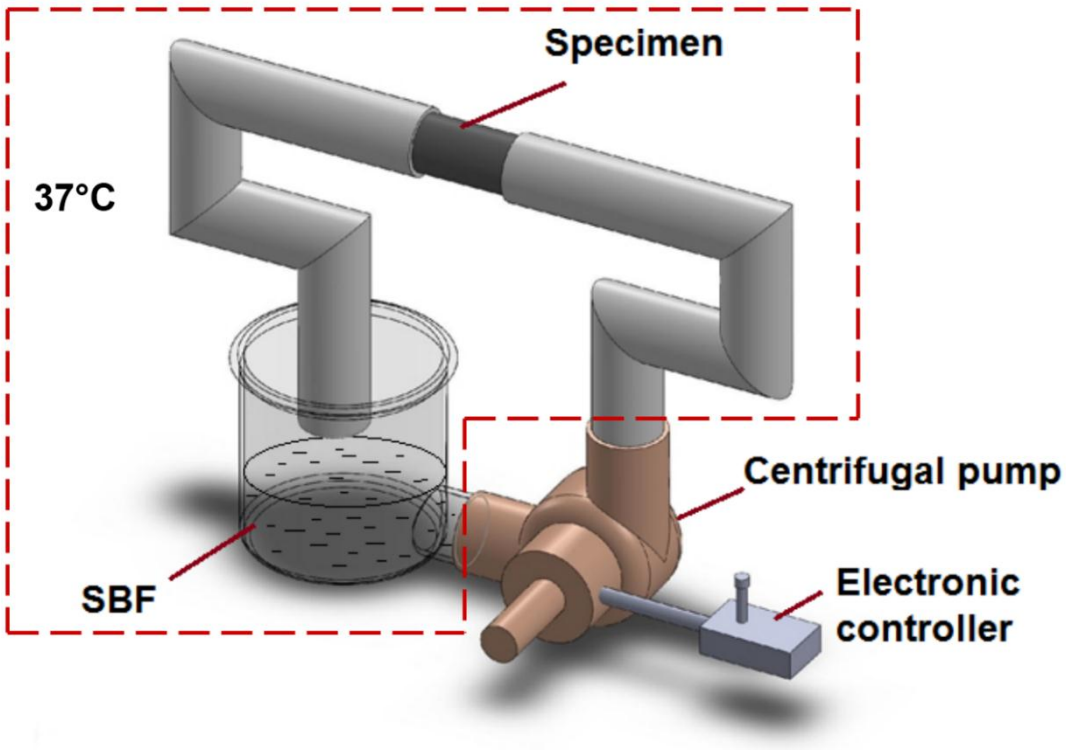

Fig. 3.3. Schematic diagram of the dynamic test platform for performing in-vitro biodegradation.

3.6 Hydrogen evolution test

A schematic of the hydrogen evolution test set-up is shown in Fig. 3.4. The specimens of dimension 10 × 10 mm^2 of the uncoated AE42 alloy, the S-coated and SP-coated alloys were placed at the bottom of a 1000 ml beaker containing 500 ml SBF solution at approximately 37±0.5°C for 168 h. The evolved hydrogen was collected in a measuring cylinder kept above the corroding specimens. The rate of hydrogen evolution was monitored continuously as a function of immersion time. Experiments were conducted in triplicate in order to examine the reproducibility of hydrogen evolution.

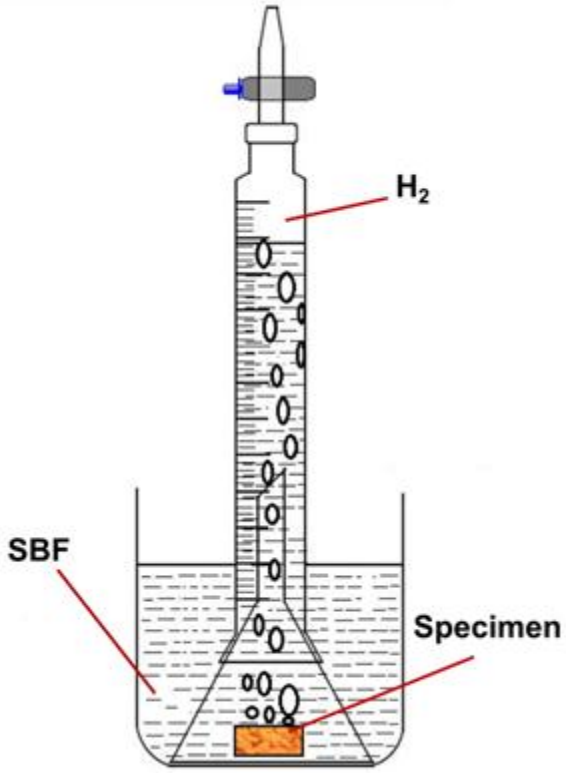

Fig. 3.4. Apparatus for the measurement of hydrogen evolved.

3.7 Electrochemical corrosion tests and its characterization

Potentiodynamic polarization scan and electrochemical impedance spectroscopy (EIS) were performed in a SBF solution using a potentiostat (Gill AC, ACM Instruments) consisting of a three electrode system. The specimen (exposed area of 0.5 cm^2) acted as working electrode, a platinum mesh acted as counter electrode and a saturated calomel electrode (SCE) was the reference electrode. 200 ml of SBF incubated in a water bath at 37±0.5ºC served as electrolyte. Open circuit potential was monitored for 300 s. Potentiodynamic polarization tests were carried out ±250 mV relative to the OCP at a scan rate of 12 mV/min. For EIS tests, a sinusoidal potential signal of 5 mV amplitude was used. The impedance response was measured over the frequencies ranging from 100 kHz and 10 mHz. The impedance spectra obtained from EIS were simulated using electrical equivalent circuits. The morphology of the corroded specimens were observed using FESEM. All the corroded specimens were gold sputter coated before observation under FESEM. XRD was also done to check the presence of

corrosion products on the coated and uncoated specimens with a scan range (2θ) from 10-80°. The scan speed was 5°/min and a step size of 0.05 was maintained.

3.8 Protein adsorption test

For protein adsorption test, bovine serum albumin (BSA) (HiMedia, India) was used as model protein. A calibration curve was drawn for standard BSA solution ranging from 200-1000 µg/ml. 25 ml of protein solution (1000 µg/ml protein/saline solution) was pipette onto the uncoated and coated specimens. The setup was allowed to remain for a period of 1, 3, 6 and 24 h separately and 1ml of protein solution was removed and centrifuged. After that 100 µl of supernatant was taken and mixed with 1 ml of Bradford reagent (HiMedia, India) and 2 ml of deionized water and kept in dark for 10 min. The absorbance was recorded at 595 nm using UV-Vis spectrometer (Perkin Elmer, Lambda 35). The protein concentration was determined using the calibration curve.

3.9 *In-vitro* hemocompatibility

3.9.1 Hemolysis test

Specimens of 10 x 10 mm^2 in dimension were cut and soaked in physiological saline (0.9% (w/v)) for 24 h at 37°C. The specimens were taken in tubes containing 10 ml physiological saline. Human blood (20 ml) with potassium citrate solution (1 ml, 1 mg/ml) was diluted up to 4/5 (v/v) with physiological saline. Then 0.5 ml of the diluted blood was added into each test tube and kept at 37°C for 1 h. For positive and negative controls 0.5 ml of blood was added in 10 ml of distilled water and physiological saline respectively. After 1 h specimens were centrifuged at 3500 rpm for 5 minutes and its optical density (OD) was taken at 545 nm. The optical density of the specimens was measured in triplicate. Percentage hemolysis ratio was calculated based on the optical density (OD) using the following formula [33]:

$$\%\ Hemolysis = \ [(OD_{test} - OD_{-ve})/(OD_{+ve} - OD_{-ve})]\ x\ 100 \qquad \ldots (1)$$

where OD_{test}, OD_{-ve} and $OD_{+ve,}$ are optical density values of test, negative control and positive control specimens respectively.

3.9.2 Platelet adhesion test

Platelet adhesion test was conducted in order to evaluate thrombogenicity of the specimens and examined the interaction between blood and the specimens *in-vitro*. For this platelet-rich plasma (PRP) was prepared by centrifuging human blood containing 3.8 wt.% sodium citrate at 1,500 rpm for 15 min. Then 60 µl of PRP was placed individually on top of each specimen, and incubated at 37ºC for 2 h. The specimens were gently rinsed with phosphate buffer solution (PBS) and 60 µl of 2.5% glutaraldehyde solution was added on to the specimens and kept for 30 min. The specimens were then dehydrated sequentially in 50%, 75%, 90% and 100% ethanol solution. The specimens were gold sputter-coated (JEOL JFC 1600 Autofine Coater), and the platelet adhesion on the coated and uncoated specimens were observed using SEM (JEOL, JSM-6084LV).

CHAPTER 4

RESULTS AND DISCUSSIONS

4.1 Characterization

4.1.1 X-ray diffraction

The XRD pattern of the squeeze-cast AE42 alloy is shown in Fig. 4.1. It is evident that the as-cast AE42 alloy consists of primary Mg (α-Mg) peaks along with the peaks corresponding to Al_4RE phase. The phases $Al_{11}RE_3$ and Al_4RE are considered to be the same and are conventionally denoted as Al_4RE phase in the literature [14, 15]. There was no peak observed corresponding to the β-$Mg_{17}Al_{12}$ phase, which is generally present in Mg-Al alloys.

4.1.2 Scanning electron microscopy

The surface morphology of the coated and uncoated specimens under FESEM is shown in Fig. 4.2. The micrograph of the uncoated specimen reveals nearly polygonal grains of α-Mg with an average grain size of 25 μm Fig. 4.2 (a). The detailed description of the microstructure is reported elsewhere [36]. It is observed from Fig. 4.2 (b) that the S-coated surface had a wavy appearance. A similar morphology of silane coating was also observed by Kelly et al. [37]. The reason behind this uneven distribution of the coating deposition is not known. In contrast,

a reasonably smooth and uniform coating morphology was observed for the SP-coated specimen as shown in Fig. 4.2 (c). There was no crack observed on the coated surfaces of the specimens even after curing. The SEM micrograph of the cross-section of the SP-coated specimen is shown in Fig. 4.3. Line scan using EDS was carried out on the coating of the specimen. It displayed the dominant presence of C along with Si and O at the coated region confirming the presence of the silane-PMMA coating. The presence of Mg as the major element at the specimen substrate was also seen.

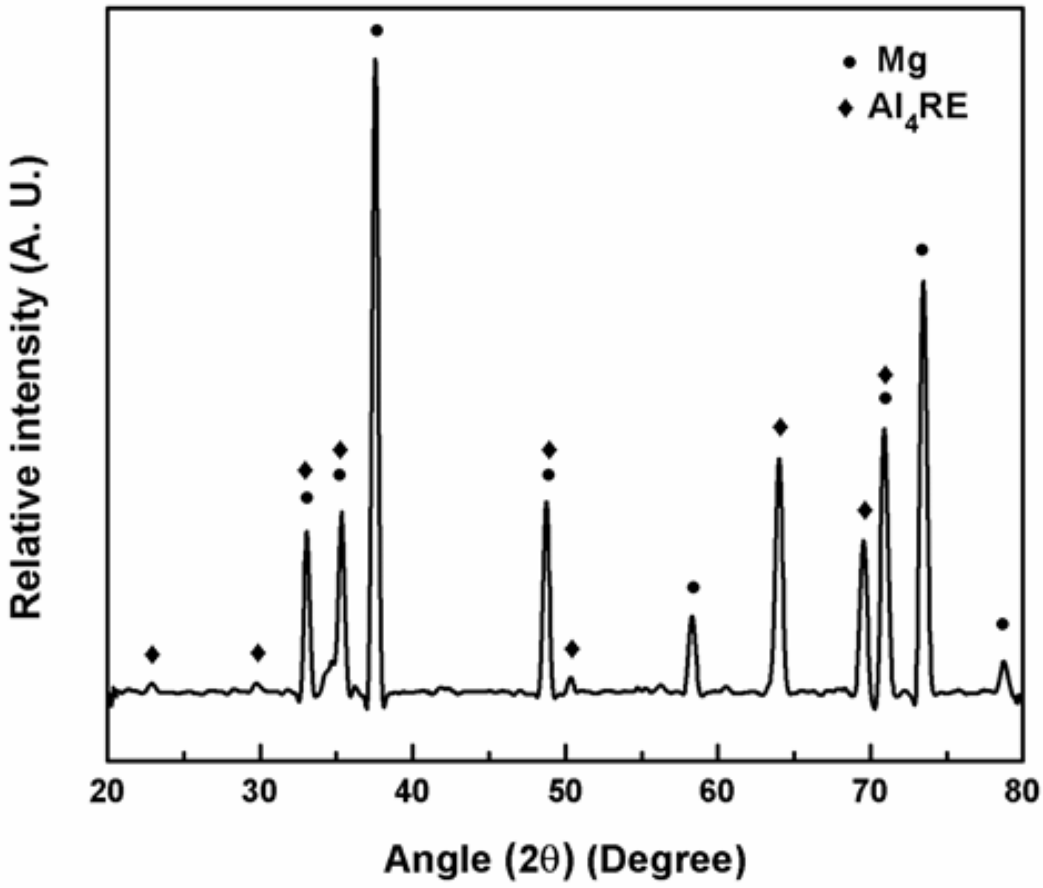

Fig. 4.1. XRD patterns obtained from the as-cast uncoated AE42 alloy.

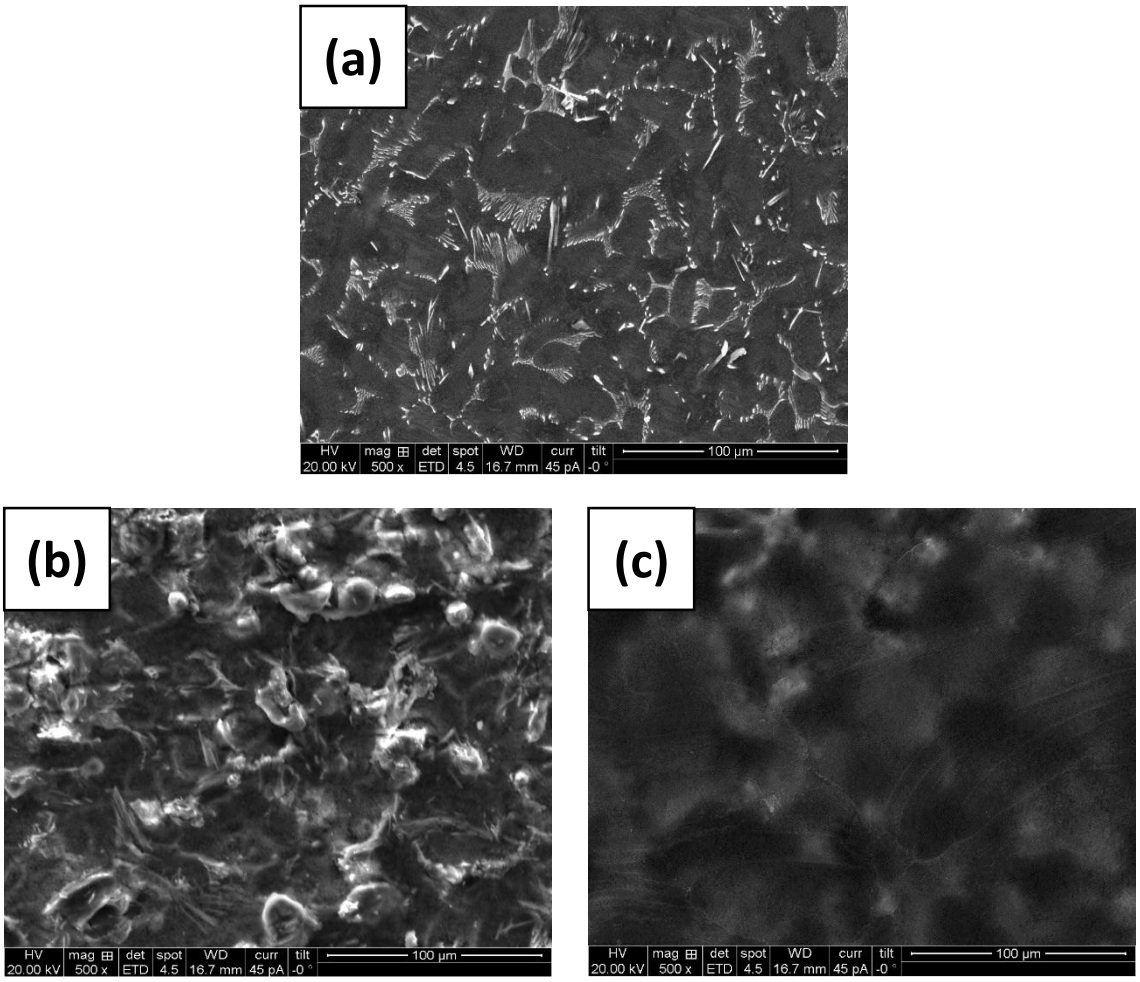

Fig. 4.2. Scanning electron micrographs of the (a) uncoated, (b) S-coated and (c) SP-coated specimens.

4.1.3 Mechanical characterization

The adhesion and pencil hardness tests were conducted on the coated surfaces of the specimens and the values are shown in Table 4.1. The adhesion test revealed strong adhesion with a rating of 5B, which is the best as per the ASTM D 3359-09 standard. The values of the pencil hardness of the coatings were 4H and 5H for the S-coated and the SP-coated specimens. Gaur et al. [5] also observed an adhesion of 5B and pencil hardness of 4H after investigating the mechanical characteristics of the silane coating on Mg-6Zn-Ca Mg alloy. The reason behind the strong adhesion is that the aminolysis reaction caused the -NH group of the silane to couple with the ester group of the PMMA. This covalent coupling attributed to

the adhesion of a firm, smooth and stable PMMA layer on the S-coated alloy specimen as shown in Fig. 7 (b).

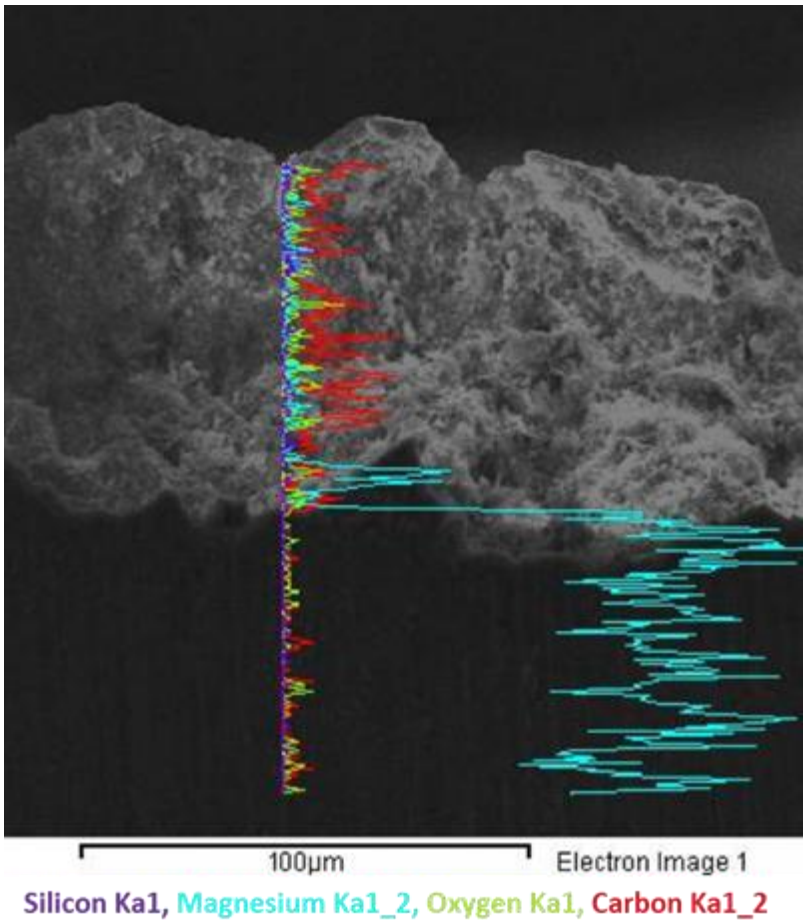

Fig. 4.3. Cross-sectional view of the silane-PMMA coating with the results of EDS line scan.

Table 4.1 Results of adhesion and hardness tests for the coatings.

Specimen	Adhesion	Hardness
S-coating	5B	4H
SP-coating	5B	5H

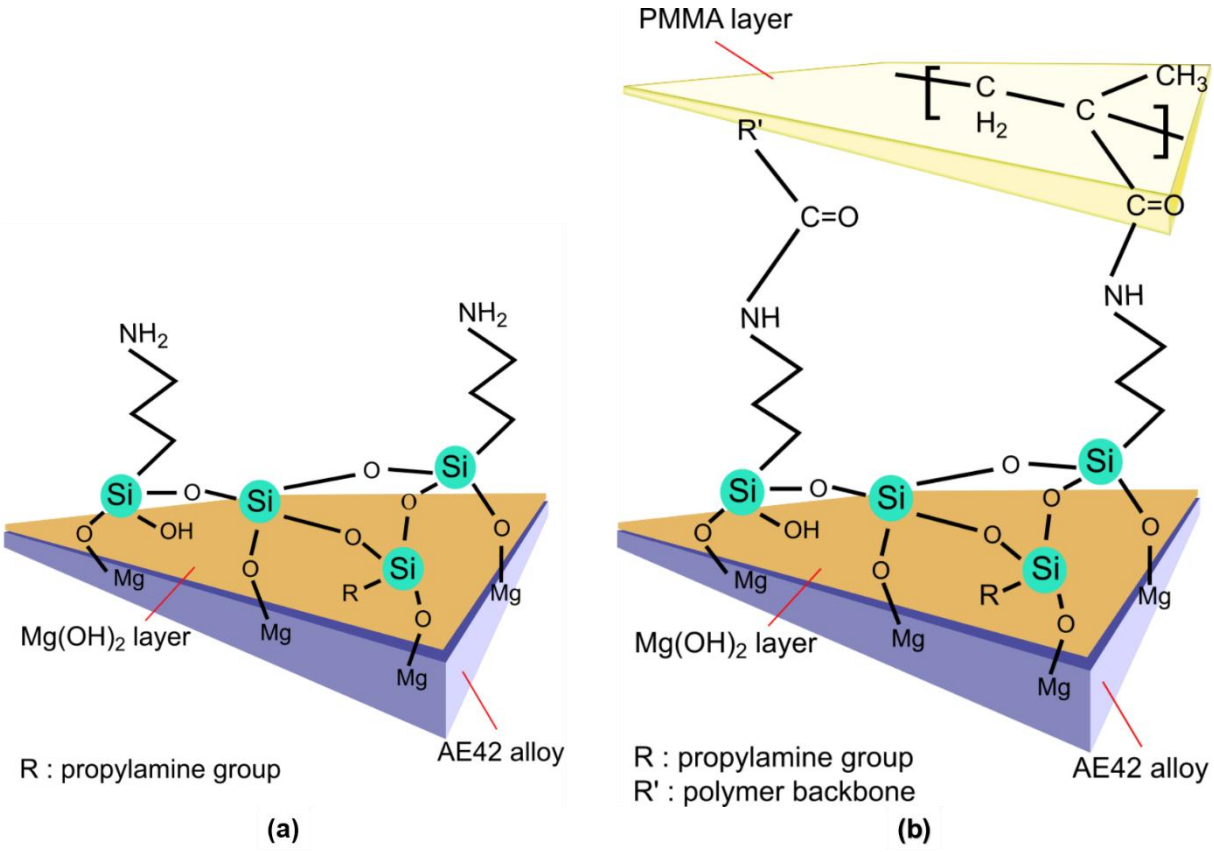

Fig. 4.4. Schematic diagram of the sol-gel coating process for (a) silane coating and (b) silane-PMMA coating on AE42 alloy.

4.1.4 Fourier transform infrared spectroscopy

The FTIR spectra obtained from the silane coating as well as silane-PMMA coating are shown in Fig. 4.5. A schematic representation of the overall reactions governing the coating process in the S-coated and SP-coated specimens in sol-gel method is shown in Fig. 4.4 (a and b). The alkali pretreatment caused strong bonding between the -OH group of the $Mg(OH)_2$ layer and Si of the APTES. The band related to the formation of OH-Mg-OH group was observed at 619 cm^{-1} [38]. The bands that appeared at ~ 1010 and 1100 cm^{-1} correspond to the asymmetric stretching of Si-O-Si linkage. It confirmed the formation of a cross-linked siloxane network in the film [19, 20]. The bands corresponding to Si-O-Et (asymmetric) and Si-OH were observed at 1389 and ~ 850 cm^{-1}, respectively. The FTIR results in the present investigation match well with the reported literature [5]. The band at 1620 cm^{-1} was attributed to the N-H bending region of free -NH_2 group owing to the presence of the amine group in the APTES [40]. The

characteristic band of the PMMA corresponding to the stretching of C=O bond was observed at 1732 cm^{-1} [41]. The broad peak at ~ 3400 cm^{-1} was assigned to the vibration of -OH group. This helped to create a Si-O-Si network (Fig. 4.4 (a)) whose presence is already confirmed by the results of FTIR.

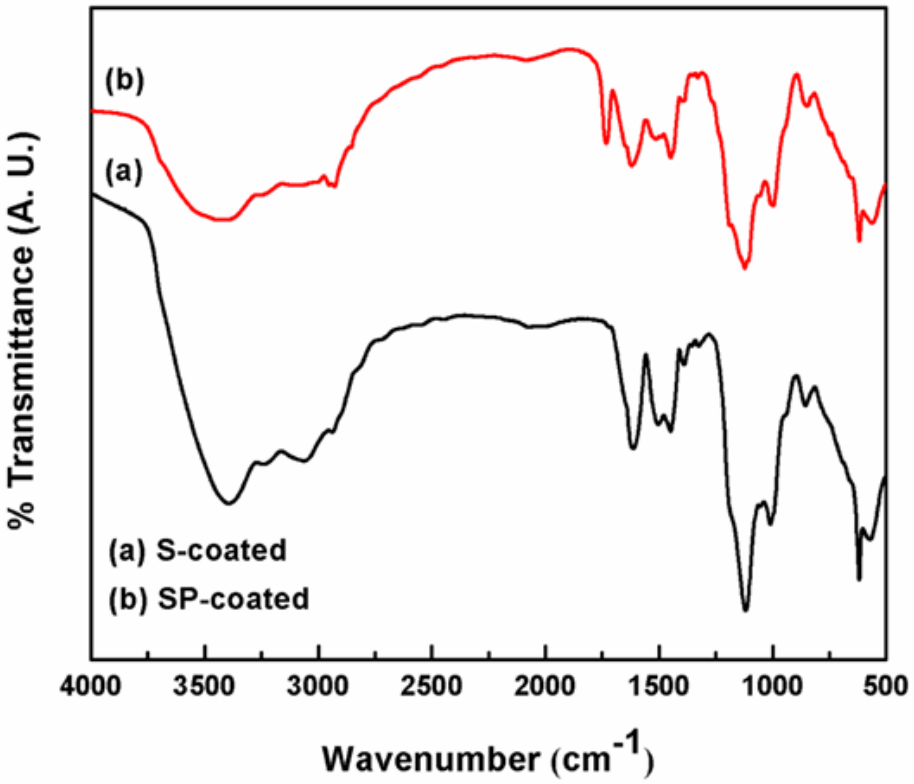

Fig. 4.5. FTIR results obtained from the coated specimens; (a) S-coated (b) SP-coated.

4.2 Surface wettability measurement

Surface wettability plays a vital role in the corrosion behavior of the specimens. Table 4.2. shows the average values of the contact angles. The contact angle for the uncoated AE42 specimen was found to be ~ 64º. Majumdar et al. [42] too observed a contact angle of 63º for the AZ91 Mg alloy. The S-coated specimen had a contact angle of ~ 83º. The increase in contact angle with the silane coating indicates the increased hydrophobicity and it was attributed to the presence of the -OH group on the surface, as shown in Fig. 4.4 (a). On the other hand, PMMA is a monopolar solid whose surface tension resulted only from the Lifshitz-van der Waals intermolecular interactions. It has free polar groups such as -COO and

-OCH_3 in which the oxygen may act as an electron donor in contact with water and form a hydrogen bond [43]. Yeh et al. [44] too showed that the incorporation of silica with PMMA increased the water contact angle and made the surface hydrophobic. A contact angle of ~ 114º for the SP-coated specimen was obtained. The wettability of the SP-coated surface decreased because the -COO group of the PMMA is already coupled to the -NH group of the silane (Fig. 4.4 (b)). This molecular level interaction between silane and PMMA helped to make the SP-coated surface inert and stable, which contributed to the hydrophobic behavior of the coating.

Table 4.2 Results of the contact angle measurement.

Specimen	Contact angle (ºDegree)
Uncoated	64.6±1.9
S-coated	83.1±5
SP-coated	113.7±1.8

4.3 *In-vitro* biodegradation test

The variation of Mg ion release as a function of time is shown in Fig. 4.6. It is quite evident from Fig. 4.6 that the testing condition decided the degradation behavior of all the specimens. The rate of degradation of all the specimens in the SI tests was significantly lower as compared to that in the DF tests. The release of the Mg^{2+} ion as well as its increase with increase in time was the lowest for SP-coated specimens employed in both SI and DF tests. In contrast, these were the highest for the uncoated specimen and intermediate for the S-coated specimen. The corrosion rate of all the specimens decreased following the formation of a passive layer in SI tests. However, the layer was washed away under the constant circulation of SBF in DF tests, which accelerated the degradation rate of the specimens. Lévesque et al. [19] too observed a similar phenomenon in AM60B alloy under dynamic flow condition. Unlike the passivized layer, the coatings acted as a barrier and provided a relatively higher

protection to Mg substrate from dissolution. The coatings under SI test conditions were able to withstand the corrosion process for a longer time as compared to the DF test conditions. This was due to the erosion additionally caused under dynamic flow condition from the constant circulation of SBF. The circulation of the SBF over the specimen surface inhibited local pH increase, and hence, a pH study was carried out to evaluate the alkaline shift in the SBF under different testing conditions.

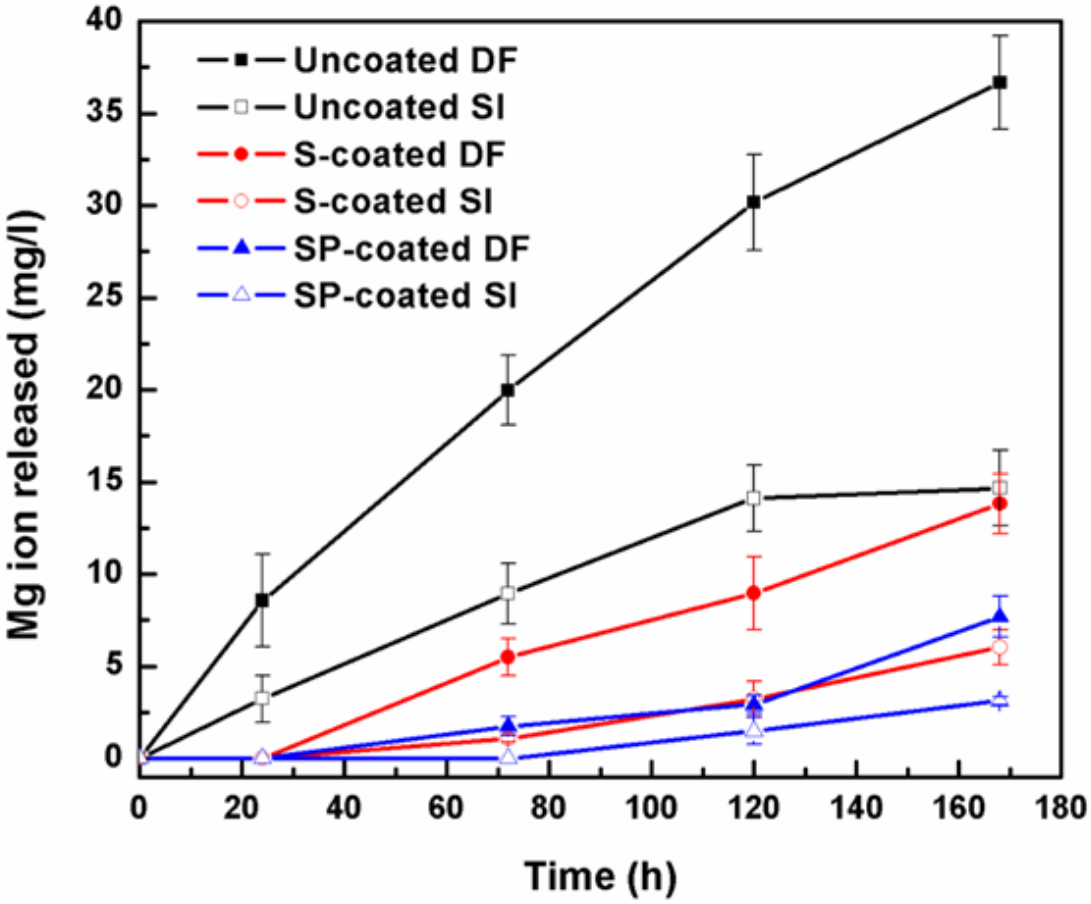

Fig. 4.6. Variation of Mg ion released with time under static immersion (SI) and dynamic flow (DF) for all the specimens.

Local alkalization unfavorably affects the pH-dependent physiological reaction in the vicinity of the Mg implant. This might even lead to an alkaline poisoning effect as the local pH exceeds 7.8 [45]. Therefore, the change in pH of the SBF solution in contact with all the specimens in SI and DF tests was recorded as a function of time and the plots are shown in

Fig. 4.7. The pH value of the SBF solution in contact with the uncoated specimen increases almost steadily with increase in time for the first 24 h. Then the rate slowed down, which might be due to the formation of passivation layer on the surface of the uncoated specimen. It was clearly visible that there was a significant difference in the pH values under SI and DF tests.

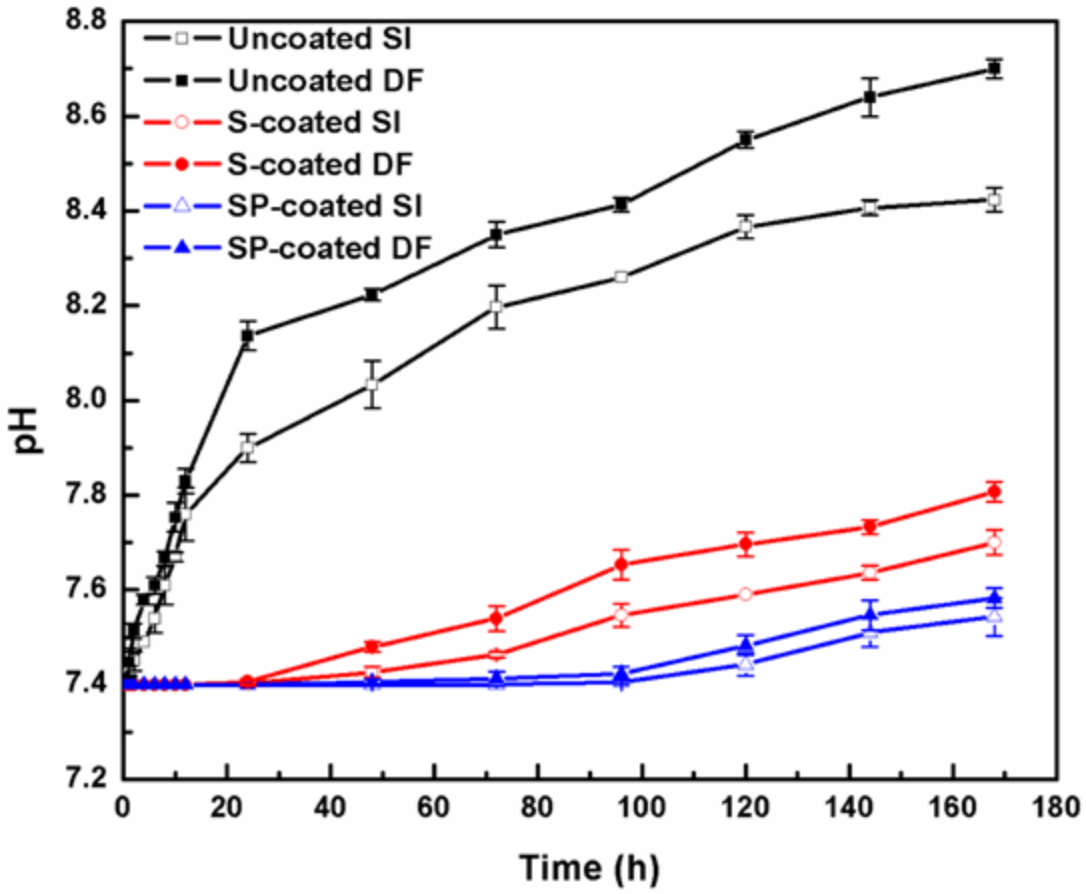

Fig. 4.7. Variation of pH with time under static immersion (SI) and dynamic flow (DF) for all the specimens.

The pH value of the SP-coated alloy after 168 h of immersion in SBF remained far below 7.8, in both SI and DF tests. Whereas, it surpassed the acceptable limit within 24 h for the uncoated specimen. The S-coated specimen also exhibited a pH value within the acceptable limit in the SI, however, it reached slightly above 7.8 in DF test. The presence of OH^- ion due

to corrosion in the SBF solution for the SP-coated specimen was the lowest and thus, bidding for the acceptability of this coating.

4.4 Hydrogen evolution test

One of the major shortcomings of using Mg as an implant material is the formation of H_2 gas when it corrodes in the body fluid by the following reaction [46]:

$$Mg + 2H_2O = Mg^{2+} + 2OH^{-} + H_2 \uparrow \quad \text{... (2)}$$

The evolved H_2 accumulates and forms gas pockets that might lead to necrosis of the neighboring tissues and delay the healing process [5]. Therefore, the H_2 evolution from all the specimens was studied with increase in exposure time and the plots are shown in Fig. 4.8.

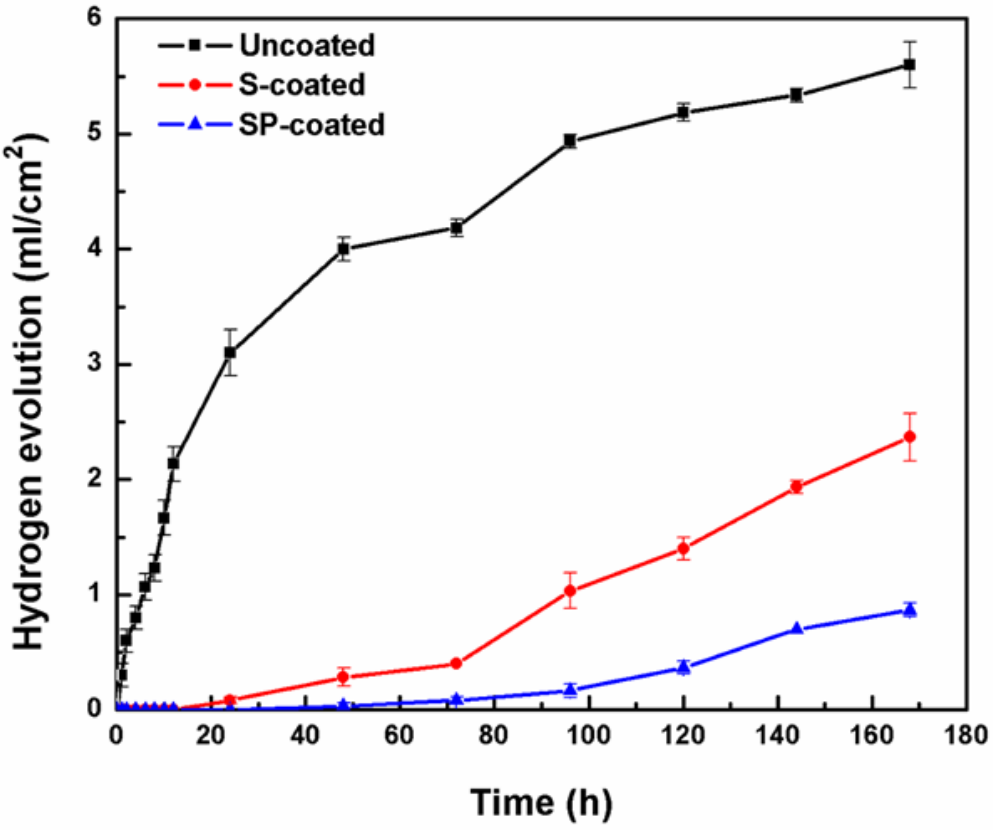

Fig. 4.8. Hydrogen evolution with immersion time for all the specimens.

It is observed that the H_2 evolution was the highest for the uncoated alloy and the lowest for the SP-coated alloy. The hydrogen evolved from the S-coated and SP-coated specimens exhibited a trend similar to that of their pH change with the increase in immersion time. The curves show that the H_2 evolved was almost negligible up to 24 h for the S-coated specimen and up to 72 h for the SP-coated specimen. Following 72 h of exposure the curve for the S-coated specimen rose moderately owing to the formation of cracks on the S-coated surface.

4.5 Electrochemical corrosion tests and its characterization

The potentiodynamic polarization curves of the uncoated, S-coated and SP-coated AE42 alloy specimens are shown in Fig. 4.9. The corrosion current, I_{corr} and the corrosion potential, E_{corr} were determined by Tafel extrapolation and the values were listed in Table 4.3. The I_{corr} value of the SP-coated specimen is three order of magnitude lower than that of the uncoated AE42 alloy, and one order lower than that of the S-coated specimen.

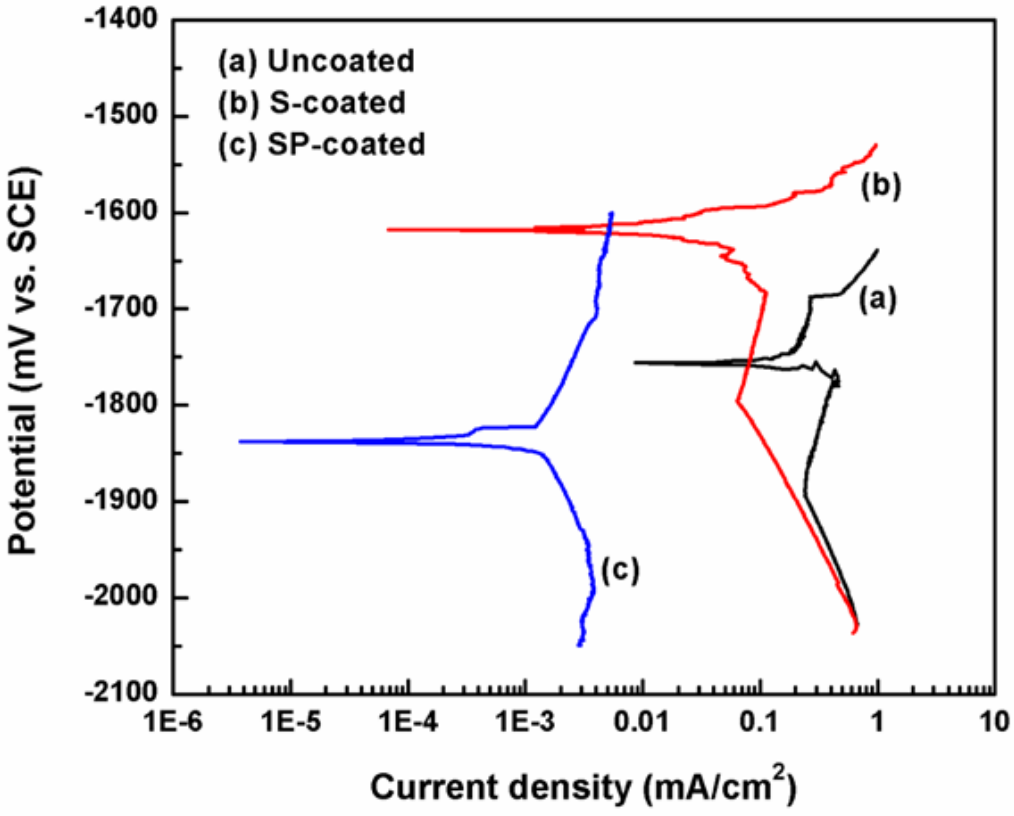

Fig. 4.9. Tafel curves obtained from potentiodynamic polarization tests for all the specimens.

The E_{corr} value of the SP-coated was lower than that of the uncoated and S-coated specimens by 83 and 221 mV, respectively. The corrosion rate determined from the potentiodynamic polarization tests is shown in Fig. 4.10.

Table 4.3 Summary of the various parameters obtained from the potentiodynamic polarization tests.

Specimen	Ecorr (mV vs. SCE)	Icorr (mA/cm^2)	Polarization Resistance ($\Omega.cm^2$)
Uncoated	-1755.5	0.1357277	260.50
S-coated	-1617.5	0.0208160	830.07
SP-coated	-1838.6	0.0009734	64770.00

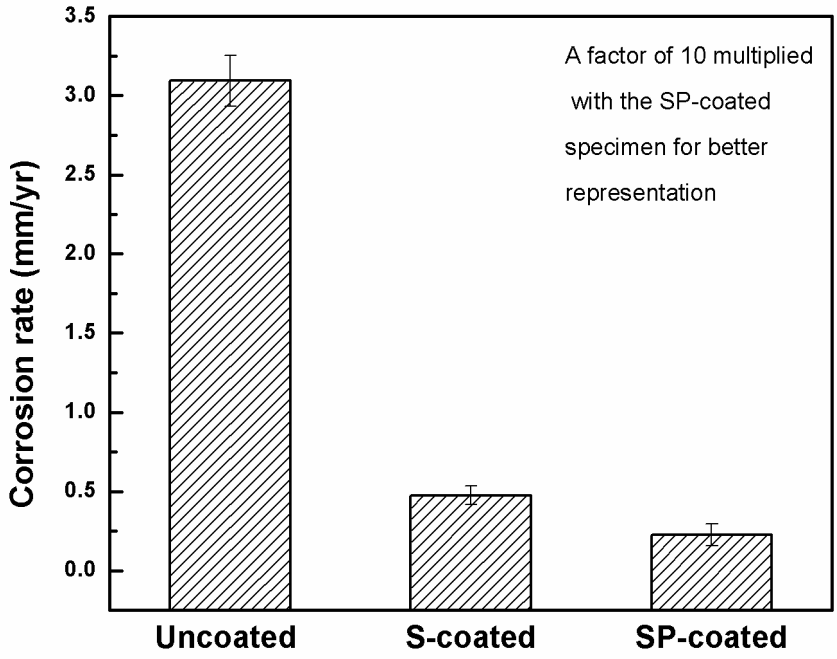

Fig. 4.10. Corrosion rates determined from the potentiodynamic polarization tests for all the specimens.

It is evident that the corrosion rate of the SP-coated specimen is two order and one order of magnitude lower than that of the uncoated and S-coated AE42 specimen, respectively. Moreover, the polarization resistance of the SP-coated specimen was two order of magnitude higher than that of the S-coated and uncoated specimens.

EIS was carried out to investigate the long-term corrosion behavior of all the specimens and the plots are shown in Fig. 4.11. It is obvious that $|Z|_{SP\text{-}coated} >> |Z|_{S\text{-}coated} > |Z|_{uncoated}$. In order to develop a greater insight into the corrosion mechanism and the corrosion resistance provided by all the specimens, electrical equivalent circuits (EEC) were simulated based on the EIS data as shown in Fig. 4.12.

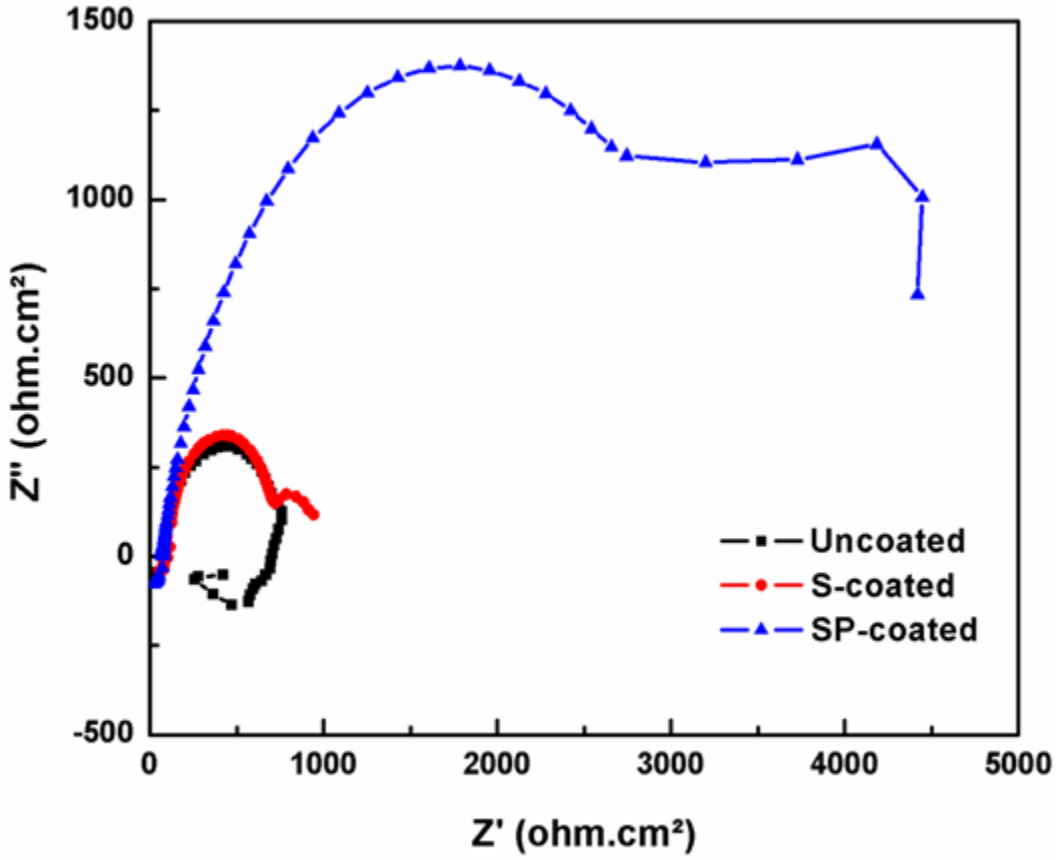

Fig. 4.11. EIS spectra obtained in SBF for all the specimens.

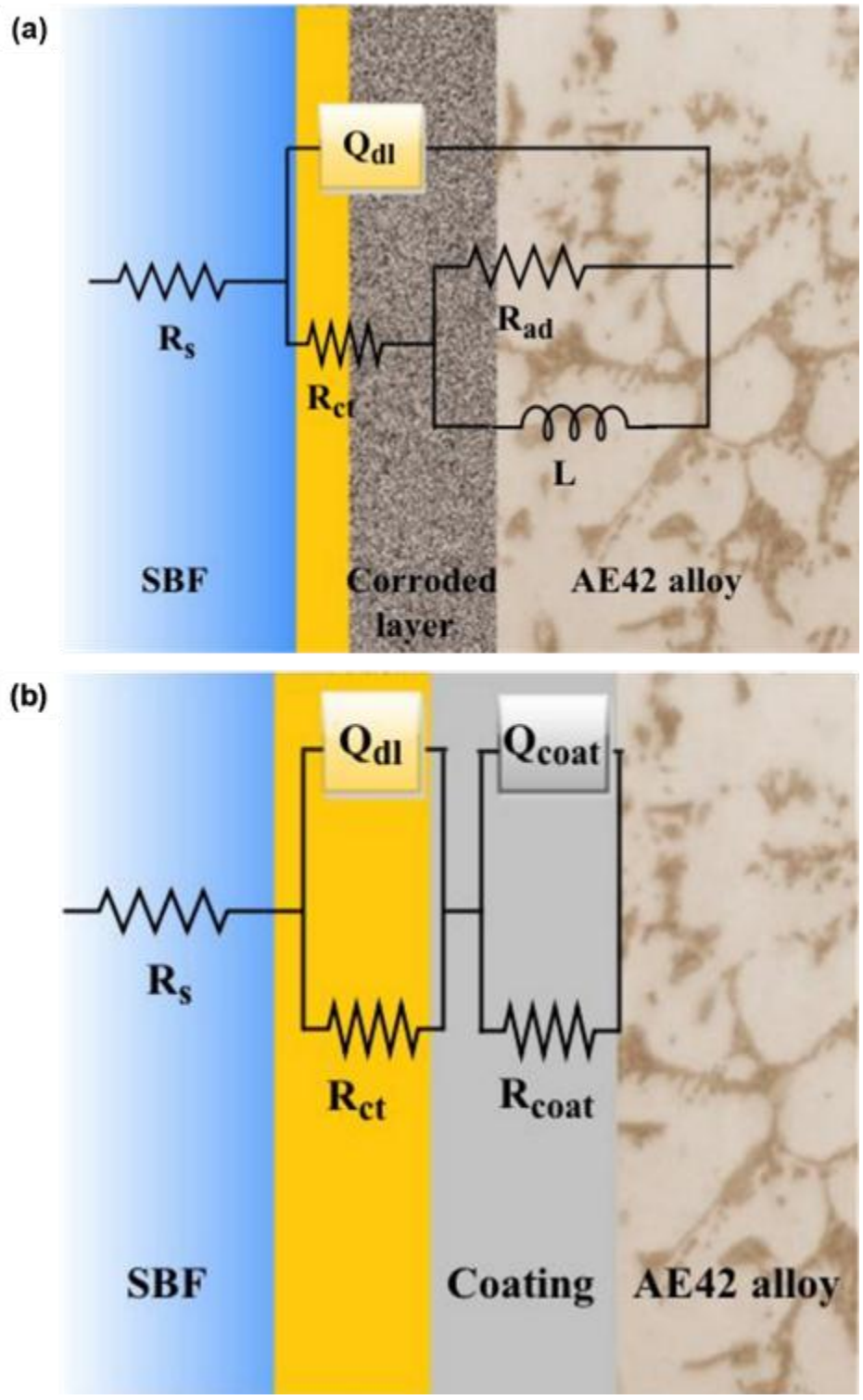

Fig. 4.12. Electrical equivalent circuit (EEC) corresponding to the EIS data obtained for the (a) uncoated and (b) the S-coated and SP-coated AE42 alloy.

The calculated data from the EEC simulation were fitted to the data obtained experimentally. The resistance offered by the SBF is denoted as R_s. R_{ct} is the resistance due to the charge transfer. A double layer capacitive zone (Q_{dl}) that formed as a result of interaction between the free electrons on the metal surface and the negative ions present in the SBF. Instead of pure capacitance, a constant phase element (CPE) was considered. This kind of consideration was reported earlier [47]. The CPE impedance is as follows [48]:

$$Z_{CPE} = Q^{-1}(j\omega)^{-n} \quad \text{... (3)}$$

where Z_{CPE} is the CPE impedance (Ω cm^2), Q is a constant (Ω^{-1} cm^{-2} sn), n is a dimensionless constant in the range $-1 \leq n \leq 1$, j is the imaginary number where $j = \sqrt{(-1)}$ and ω is the angular frequency ($\omega = 2\pi f$, f is the frequency). There could be two reasons behind the observed inductive behavior of the uncoated alloy shown in Fig. 4.11. First, the adsorption of Mg^{2+} species through the $Mg(OH)_2$ corrosion layer [49]. Second, the presence of magnetic properties of the rare earth elements. The inductive behavior is denoted by L and the resistance provided due to the adsorption of Mg^{2+} species through the intermediate porous corrosion layer is given by R_{ad}. The dual semicircles observed in the Nyquist plots of both the coated specimens were attributed to the coating barrier. As a result, separate EEC was modelled and fitted to those curves. The capacitive loop created due to the coatings, consists of a CPE denoted by Q_{coat} and resistance offered by the coatings denoted by R_{coat} as shown in Fig. 4.12 (b). The various parameters employed to fit EEC are shown in Table 4.4.

Table 4.4 Summary of the parameters obtained from the EEC fitting.

Specimen	R_{ct} **(Ω.cm^2)**	Q_{dl} **(Ω^{-1}.cm^{-2} sn)**	L **(Henri.cm^2)**	R_{ad} **(Ω.cm^2)**	R_{coat} **(Ω.cm^2)**	Q_{coat} **(Ω^{-1}.cm^{-2}sn)**
Uncoated	258	4.022×10^{-6}	87.7	232	-	-
S-coated	538.6	3.56×10^{-6}	-	-	266.4	175.9×10^{-5}
SP-coated	2151	445.6×10^{-6}	-	-	2851	1.73×10^{-5}

It is worth noting that R_{ct} was the lowest for the uncoated specimen and it increased by two folds for the S-coated specimen and by seven folds for the SP-coated specimen. Also, R_{coat} for

the SP-coated specimen was higher by an order as compared to that of the S-coated specimen. This indicated that the protection provided by the silane-PMMA coating was much higher relative to that provided by the silane coating alone.

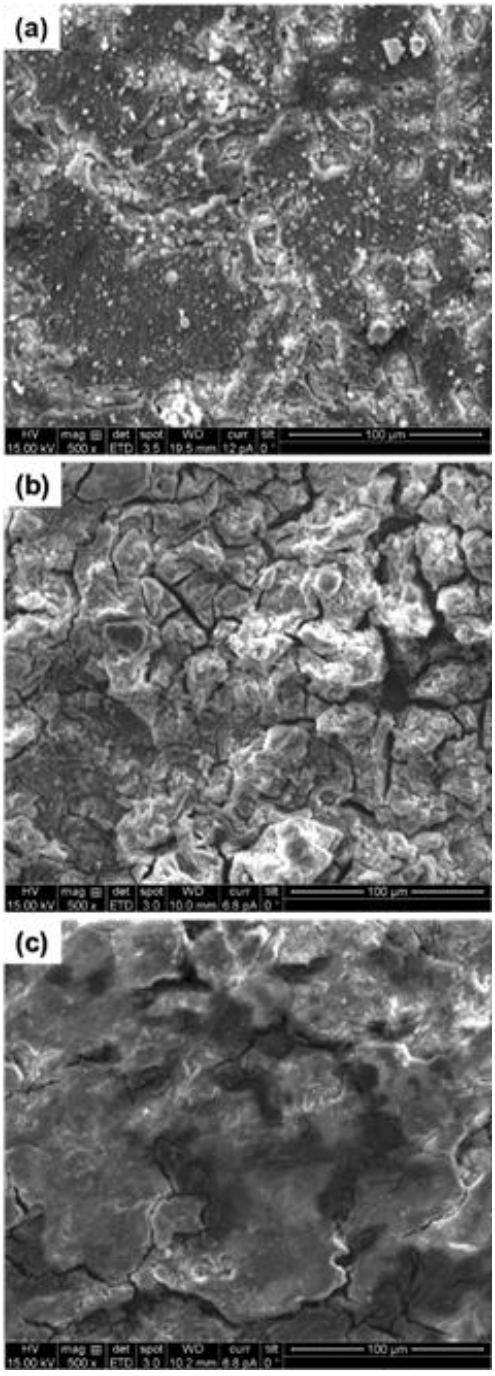

Fig. 4.13. SEM micrographs of the corroded surfaces of the (a) uncoated, (b) S-coated and (c) SP-coated AE42 alloy.

Fig. 4.13 shows the SEM micrographs of the uncoated, S-coated and SP-coated AE42 alloy specimens after 168 h of immersion in SBF. It is clearly visible that the surface of the uncoated specimen was degraded deeply at some areas showing substantial signs of corrosion (Fig. 4.13 (a)). The surface of the S-coated specimen revealed a network of cracks exposing the base alloy at some areas (Fig. 4.13 (b)), whereas, the SP-coated specimen exhibited very few shallow micro cracks indicating minimal damage to the surface (Fig. 4.13 (c)).

The XRD patterns obtained from the corroded surfaces of all the specimens are shown in Fig. 4.14. The presence of $Mg(OH)_2$ was identified as corrosion product in the uncoated and S-coated specimens. $Mg(OH)_2$ peaks were dominantly observed on the uncoated alloy surface due to the exposure of α-Mg to corrosion at surface.

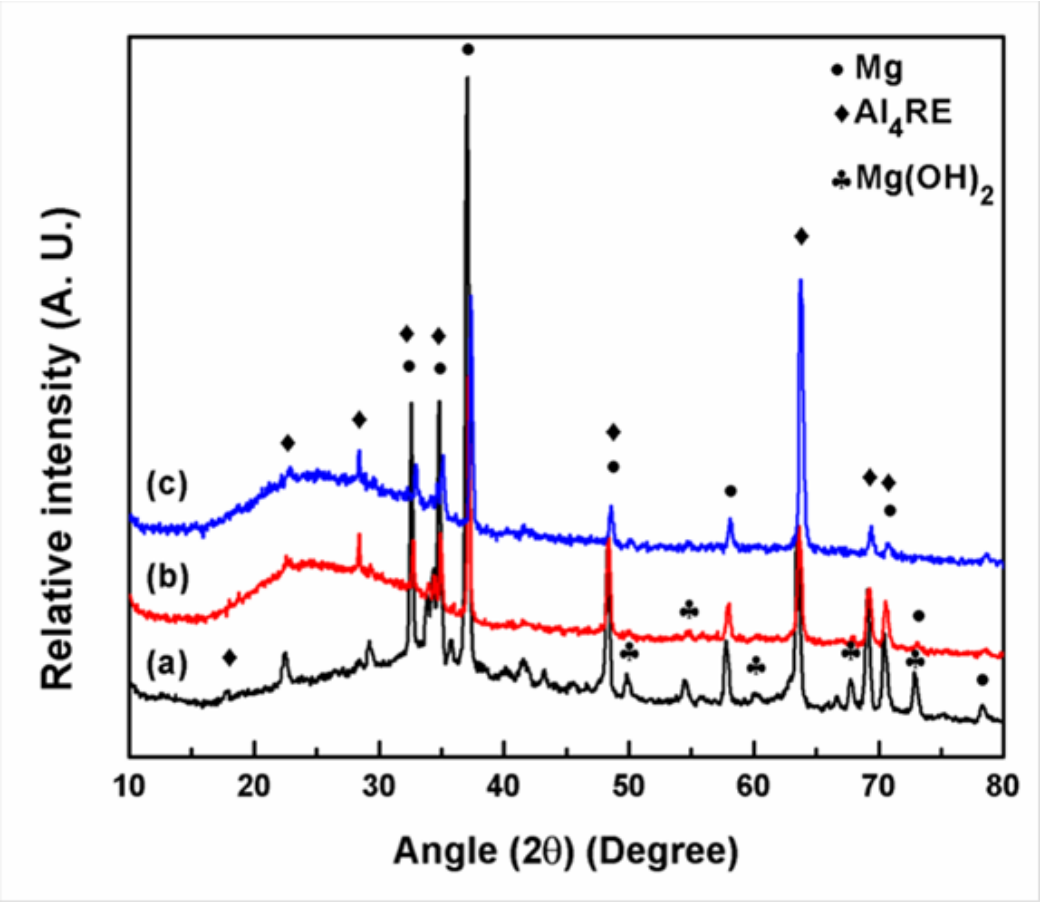

Fig. 4.14. XRD patterns obtained from the corroded surfaces of all the specimens after 168 h immersion in SBF (a) uncoated, (b) S-coated and (c) SP-coated AE42 alloy.

The presence of the $Mg(OH)_2$ on the S-coated specimen was very minimum owing to the presence of shallow microcracks on the S-coated specimen. No $Mg(OH)_2$ peak was observed for the SP-coated specimen indicating least corrosion of the surface. The results obtained from *in-vitro* biodegradation and hydrogen evolution tests also displayed that the SP-coated specimens have excellent resistance to corrosion and biodegradation in SBF over other specimens.

4.6 Protein adsorption studies

Protein adsorption is an essential criterion that estimates the adhesion of cells on the specimen surface. The tailoring of specimen surfaces highly influences the protein adsorption. BSA was selected for this study since albumin is the most abundant protein present in the human blood plasma [50]. The variation of protein adsorbed on the surfaces of the specimens was measured as a function of time and is shown in Fig. 4.15.

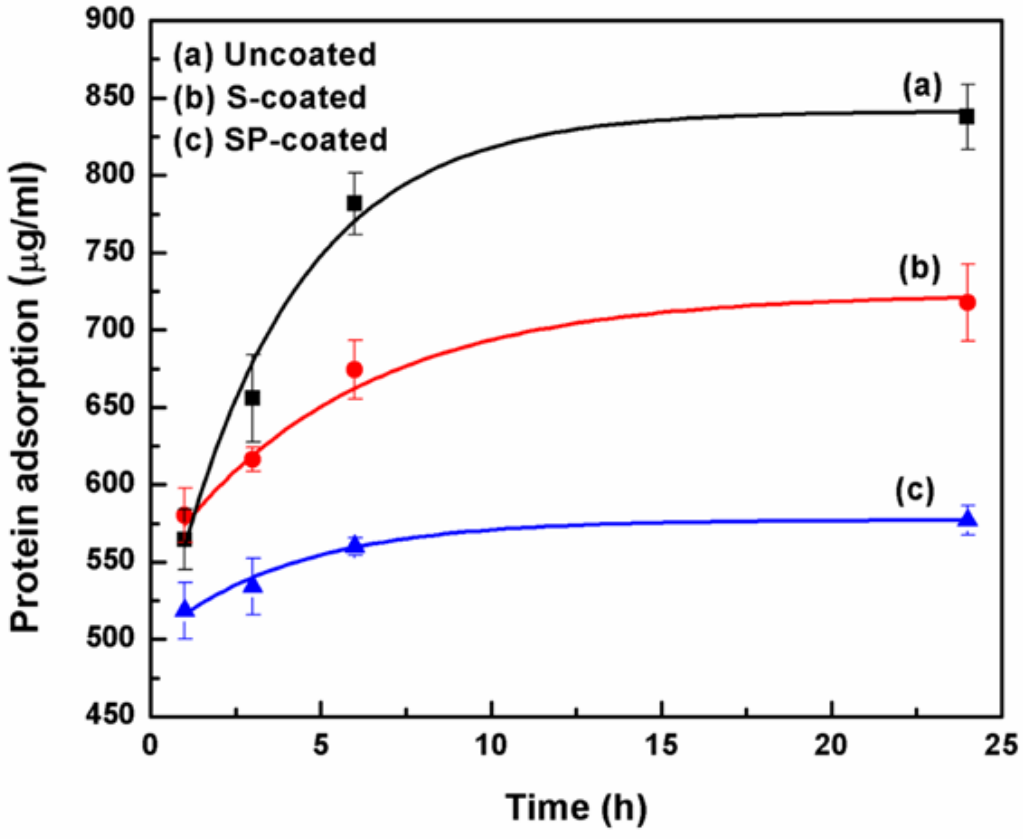

Fig. 4.15. Protein adsorbed as a function of time for all the specimens.

From the figure, it is observed that initially the protein adsorption increases exponentially with increase in time and then started stabilizing after 6 h of incubation. Yang et al. [51] too reported an exponential trendline of protein adsorption kinetics tested with albumin and fibronectin on Ti surface. After 3 h of incubation, the protein adsorbed on the uncoated alloy specimen was higher than that of the S-coated and SP-coated specimens by 5.5 and 19.2%, respectively. The protein adsorption after the attainment of the steady state following 24 h of incubation on the uncoated specimen surface was found to increase by 14.67 and 38.54% respectively for the S-coated and SP-coated specimens. Therefore, the adsorption of protein on the specimen surfaces decreased with the corresponding decrease of their wettability. This also indicated a lower affinity of the BSA to adsorb on hydrophobic surfaces as compared to hydrophilic surfaces. This opinion is in agreement with the observation of Roach et al. [50]. In addition, the corrosion resistance of the specimens improved as the hydrophobicity of the surface improved [44]. In the context of a cardiovascular stent, the protein adsorption and surface wettability of the specimen surfaces might also provide an assessment about the platelet adhesion on the surfaces of the specimen for which hemocompatibility tests were further carried out.

4.7 *In-vitro* Hemocompatibility

4.7.1 Hemolysis test

Table 4.5 shows the hemolytic ratio (HR) obtained from the hemolytic activity of the specimens. The HR values of the S-coated and the SP-coated specimens were 0.220 and 0.013% exhibiting no hemolytic activity. The uncoated specimen had an HR value of 4.260% that lied within the acceptable limit for clinical applications i.e., below 5% [52]. The HR values correlate with the corrosion behavior of the specimens. The concentration of Mg^{2+} ions in the blood plasma released due to corrosion had an adverse hemolytic effect. As the Mg^{2+} concentration is increased, the osmotic pressure of the solution is also enhanced. This caused swelling of the erythrocytes followed by the rupture of their cell membrane, which finally lead to the hemolysis of red blood cells [53]. In addition, the degradation of Mg produced OH^{-} ion in the blood plasma. This increased the pH value of the blood, which enhances hemolytic activity. The Mg^{2+} ion release as well as the variation of pH value was the highest for the

uncoated specimen and the lowest for the SP-coated specimen with the S-coated specimen showing intermediate values. The synchronization of Mg^{2+} ion release and the variation of pH value were directly related to the corrosion behavior of the specimens, which decided their hemolytic activity. In other words, higher is the resistance to corrosion of the specimens lower is the Mg^{2+} ion release that causes a minor increase in pH value and therefore, the hemolytic activity is controlled.

Table 4.5 Results of hemolysis tests on the specimens.

Specimen	Hemolysis Ratio (%)
Uncoated	4.260±0.270
S-coated	0.220±0.110
SP-coated	0.013±0.004

4.7.2 Platelet adhesion test

As per Goodman's observations, a platelet spreading can be divided into five categories for analysis: round, dendritic, spread dendritic, spread and fully spread [54]. A platelet with dendritic spreading having pseudopodial projections was observed (Fig. 4.16 (a)), which showed signs of platelet activation on the uncoated alloy surface. The S-coated specimen showed few platelets adhered on its surface (Fig. 4.16 (b)). A platelet having a dendritic morphology was clearly visible. On the other hand, very few platelets were detected on the SP-coated specimen surface and their morphology was observed to be in the round state, i.e., there was no sign of activation (Fig. 4.16 (c)). It is evident that there were a larger number of adherent platelets on the uncoated alloy surface as compared to that on the surfaces of coated alloys. The AE42 alloy has a weak propensity of platelet activation which was attributed to the presence of rare earth elements. Vogler et al. [55] indicated that the plasma coagulation induced by a hydrophobic surface is much less as compared to a hydrophilic surface. The adhesion of platelets for the specimens behaved correspondingly in the order of their surface

wettability. As the surface wettability of the specimens was decreased, a decrease in the number of platelets adhered was observed.

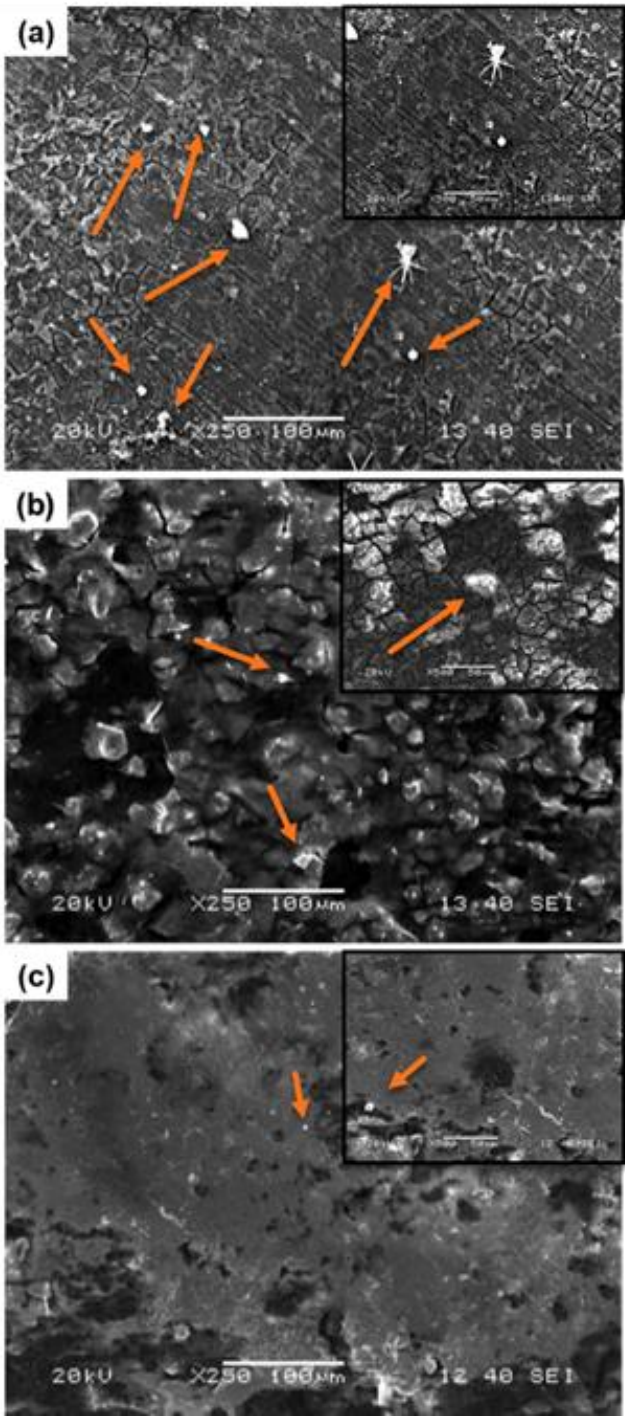

Fig. 4.16. SEM micrographs after static platelet incubation on the surfaces of (a) uncoated, (b) S-coated and (c) SP-coated AE42 alloy.

Additionally, the protein adsorption kinetics also played a crucial role in the platelet adhesion process. A rapid adsorption of proteins might cause a higher number of platelet adhesion which can trigger thrombus formation by platelet activation. This would ultimately result in blood coagulation. Hence, it can be concluded that the thrombogenicity of the specimens gradually decreased from the uncoated to S-coated to SP-coated specimen and it is in well agreement with the results obtained from their surface wettability and the protein adsorption kinetics.

CHAPTER 5

CONCLUSION

AE42 alloy was squeeze-cast and coated with silane and silane-PMMA. The coated surfaces showed improvement in their hydrophobicity, where the SP-coated specimen exhibited the least surface wettability. The *in-vitro* biodegradation test suggested that the silane-PMMA coating delayed the commencement of the degradation process by 72 h. A comparative study of the corrosion resistance revealed that the SP-coated specimen exhibited superior corrosion resistance than the S-coated and uncoated specimens by three order and one order of magnitude respectively. It was also found that protein adsorbed on the specimen surface decreased with the increase in their hydrophobicity. The hemocompatibility results showed that the hemolysis ratio for the SP-coated specimen was quite insignificant, showing no hemolytic behavior when compared to other specimens. Furthermore, the SP-coated specimens also exhibited higher resistance to thrombogenicity as compared to the S-coated and uncoated specimens. From the overall results, the SP-coated AE42 alloy specimen shows high potential material for cardiovascular stent application owing to its reasonably high resistance to biodegradation, corrosion resistance and hemocompatibility. However, further *in-vivo* studies are to be assessed before clinical trials.

REFERENCES

[1] Wang J, He Y, Maitz MF, Collins B, Xiong K, Guo L, et al. A surface-eroding poly(1,3-trimethylene carbonate) coating for fully biodegradable magnesium-based stent applications: Toward better biofunction, biodegradation and biocompatibility. Acta Biomater 2013;9:8678–89. doi:10.1016/j.actbio.2013.02.041.

[2] Mani G, Feldman MD, Patel D, Agrawal CM. Coronary stents: A materials perspective. Biomaterials 2007;28:1689–710. doi:10.1016/j.biomaterials.2006.11.042.

[3] Chen Y, Xu Z, Smith C, Sankar J. Recent advances on the development of magnesium alloys for biodegradable implants. Acta Biomater 2014. doi:10.1016/j.actbio.2014.07.005.

[4] Hornberger H, Virtanen S, Boccaccini a. R. Biomedical coatings on magnesium alloys - A review. Acta Biomater 2012;8:2442–55. doi:10.1016/j.actbio.2012.04.012.

[5] Gaur S, Singh Raman RK, Khanna a. S. *In vitro* investigation of biodegradable polymeric coating for corrosion resistance of Mg-6Zn-Ca alloy in simulated body fluid. Mater Sci Eng C 2014;42:91–101. doi:10.1016/j.msec.2014.05.035.

[6] Zucchi F, Grassi V, Frignani a., Monticelli C, Trabanelli G. Influence of a silane treatment on the corrosion resistance of a WE43 magnesium alloy. Surf Coatings Technol 2006;200:4136–43. doi:10.1016/j.surfcoat.2005.02.073.

[7] Staiger MP, Pietak AM, Huadmai J, Dias G. Magnesium and its alloys as orthopedic biomaterials: A review. Biomaterials 2006;27:1728–34. doi:10.1016/j.biomaterials.2005.10.003.

[8] Makar G, Kruger J. Corrosion of Magnesium. Int Mater Rev 1993;3:138–53.

[9] Song G, Atrens A. Corrosion Mechanisms of Magnesium Alloys. Adv Eng Mater 2000:11–33.

[10] Song Y, Shan D, Chen R, Han EH. Effect of second phases on the corrosion behaviour of wrought Mg-Zn-Y-Zr alloy. Corros Sci 2010;52:1830–7. doi:10.1016/j.corsci.2010.02.017.

[11] Zeng RC, Zhang J, Huang WJ, Dietzel W, Kainer KU, Blawert C, et al. Review of studies on corrosion of magnesium alloys. Trans Nonferrous Met Soc China (English Ed 2006;16. doi:10.1016/S1003-6326(06)60297-5.

[12] Aung NN, Zhou W. Effect of grain size and twins on corrosion behaviour of AZ31B magnesium alloy. Corros Sci 2010;52:589–94. doi:10.1016/j.corsci.2009.10.018.

[13] Ghali E, Dietzel W, Kainer KU. General and localized corrosion of magnesium alloys: A critical review. J Mater Eng Perform 2013;22:2875–91. doi:10.1007/s11665-013-0730-9.

[14] Song BG, Atrens A. Understanding Magnesium Corrosion A Framework for Improved Alloy Performance ** 2003:837–58. doi:10.1002/adem.200310405.

[15] Bobby Kannan M, Dietzel W, Raman RKS, Lyon P. Hydrogen-induced-cracking in magnesium alloy under cathodic polarization. Scr Mater 2007;57:579–81. doi:10.1016/j.scriptamat.2007.06.019.

[16] Ben-Hamu G, Eliezer D, Dietzel W, Shin KS. Stress corrosion cracking of new Mg-Zn-Mn wrought alloys containing Si. Corros Sci 2008;50:1505–17. doi:10.1016/j.corsci.2008.02.012.

[17] Bobby Kannan M, Singh Raman RK. Evaluating the stress corrosion cracking susceptibility of Mg-Al-Zn alloy in modified-simulated body fluid for orthopaedic implant application. Scr Mater 2008;59:175–8. doi:10.1016/j.scriptamat.2008.03.001.

[18] Chen Y, Zhang S, Li J, Song Y, Zhao C, Zhang X. Dynamic degradation behavior of MgZn alloy in circulating m-SBF. Mater Lett 2010;64:1996–9. doi:10.1016/j.matlet.2010.06.011.

[19] Lévesque J, Hermawan H, Dubé D, Mantovani D. Design of a pseudo-physiological test bench specific to the development of biodegradable metallic biomaterials. Acta Biomater 2008;4:284–95. doi:10.1016/j.actbio.2007.09.012.

[20] Choudhary L, Singh Raman RK. Magnesium alloys as body implants: Fracture mechanism under dynamic and static loadings in a physiological environment. Acta Biomater 2012;8:916–23. doi:10.1016/j.actbio.2011.10.031.

[21] Chou DT, Hong D, Saha P, Ferrero J, Lee B, Tan Z, et al. *In vitro* and in vivo corrosion, cytocompatibility and mechanical properties of biodegradable Mg-Y-Ca-Zr alloys as implant materials. Acta Biomater 2013;9:8518–33. doi:10.1016/j.actbio.2013.06.025.

[22] Hort N, Huang Y, Fechner D, Störmer M, Blawert C, Witte F, et al. Magnesium alloys as implant materials-Principles of property design for Mg-RE alloys. Acta Biomater 2010;6:1714–25. doi:10.1016/j.actbio.2009.09.010.

[23] Hu J, Li Q, Zhong X, Li L, Zhang L. Organic coatings silane-based for AZ91D magnesium alloy. Thin Solid Films 2010;519:1361–6. doi:10.1016/j.tsf.2010.09.014.

[24] Chen Y, Song Y, Zhang S, Li J, Zhao C, Zhang X. Interaction between a high purity magnesium surface and PCL and PLA coatings during dynamic degradation. Biomed Mater 2011;6:25005.

[25] Feil F, Fürbeth W, Schütze M. Purely inorganic coatings based on nanoparticles for magnesium alloys. Electrochim Acta 2009;54:2478–86. doi:10.1016/j.electacta.2008.07.050.

[26] Shi P, Ng WF, Wong MH, Cheng FT. Improvement of corrosion resistance of pure magnesium in Hanks' solution by microarc oxidation with sol-gel TiO2 sealing. J Alloys Compd 2009;469:286–92. doi:10.1016/j.jallcom.2008.01.102.

[27] Roy A, Singh SS, Datta MK, Lee B, Ohodnicki J, Kumta PN. Novel sol-gel derived calcium phosphate coatings on Mg4Y alloy. Mater Sci Eng B Solid-State Mater Adv Technol 2011;176:1679–89. doi:10.1016/j.mseb.2011.08.007.

[28] Li JN, Cao P, Zhang XN, Zhang SX, He YH. *In vitro* degradation and cell attachment of a PLGA coated biodegradable Mg-6Zn based alloy. J Mater Sci 2010;45:6038–45. doi:10.1007/s10853-010-4688-9.

[29] Tezuka T, Tadanaga K, Hayashi A, Tatsumisago M. Inorganic-organic hybrid membranes with anhydrous proton conduction prepared from 3-aminopropyltriethoxysilane and sulfuric acid by the sol-gel method. J Am Chem Soc 2006;128:16470–1. doi:10.1021/ja066345k.

[30] Astm_D3359-07. Standard Test Methods for Measuring Adhesion by Tape Test 2013:1–7. doi:10.1520/D3359-09E02.2.

[31] Coatings R. Standard Test Method for Film Hardness by Pencil Test 1 2010:5–7. doi:10.1520/D3363-05.2.

[32] Kokubo T, Takadama H. How useful is SBF in predicting in vivo bone bioactivity? Biomaterials 2006;27:2907–15. doi:10.1016/j.biomaterials.2006.01.017.

[33] Li XM, Li HZ, Wang SP, Huang HM, Huang HH, Ai HJ, et al. MRI-compatible Nb-60Ta-2Zr alloy used for vascular stents: Haemocompatibility and its correlation with protein adsorption. Mater Sci Eng C 2014;42:385–95. doi:10.1016/j.msec.2014.05.051.

[34] Powell BR, Rezhets V, Balogh MP, Waldo RA. Microstructure and Creep Behavior in AE42 Magnesium Die-Casting Alloy 2002.

[35] Mondal AK, Kumar S. Impression creep behaviour of magnesium alloy-based hybrid composites in the longitudinal direction. Compos Sci Technol 2008;68:3251–8. doi:10.1016/j.compscitech.2008.08.007.

[36] Mondal a. K, Blawert C, Kumar S. Corrosion behaviour of creep-resistant AE42 magnesium alloy-based hybrid composites developed for powertrain applications. Mater Corros 2015:n/a – n/a. doi:10.1002/maco.201408071.

[37] Kelly DN, Wakabayashi RH, Stacy AM. A Modi fi ed Sol − Gel Technique for Pore Size Control in Porous Aluminum Oxide Nanowire Templates 2014:4–11.

[38] Parthasarathy G, Chandra U. SPECTRSOCOPIC AND HIGH PRESSURE INVESTIGATION ON ANTIGORITE FROM THE ARARKI (L5) CHONDRITE : IMPLICATIONS FOR DETERMINATION OF THE PEAK METAMORPHIC PRESSURE. 46th Lunar Planet. Sci. Conf. Woodlands, Texas, USA; 03/2015, vol. 5, 2015, p. 8–9.

[39] Lu X, Zuo Y, Zhao X, Tang Y. The improved performance of a Mg-rich epoxy coating on AZ91D magnesium alloy by silane pretreatment. Corros Sci 2012;60:165–72. doi:10.1016/j.corsci.2012.03.041.

[40] Maity D, Chandrasekharan P, Feng S, Jun D. Synthesis and Studies of APTES Functionalized Magnetite Nanoparticles 2010:94–7.

[41] Sathish S, Chandar Shekar B. Preparation and characterization of nano scale PMMA thin films. Indian J Pure Appl Phys 2014;52:64–7.

[42] Majumdar JD, Bhattacharyya U, Biswas a., Manna I. Studies on thermal oxidation of Mg-alloy (AZ91) for improving corrosion and wear resistance. Surf Coatings Technol 2008;202:3638–42. doi:10.1016/j.surfcoat.2008.01.004.

[43] Krawczyk J, Szymczyk K, Zdziennicka A, Jańczuk B. Wettability of polymers by aqueous solution of binary surfactants mixture with regard to adhesion in polymer-solution system II. Critical surface tension of polymers wetting and work of adhesion. Int J Adhes Adhes 2013;45:106–11. doi:10.1016/j.ijadhadh.2013.05.002.

[44] Yeh JM, Weng CJ, Liao WJ, Mau YW. Anticorrosively enhanced PMMA-SiO2 hybrid coatings prepared from the sol-gel approach with MSMA as the coupling agent. Surf Coatings Technol 2006;201:1788–95. doi:10.1016/j.surfcoat.2006.03.011.

[45] Song G. Control of biodegradation of biocompatable magnesium alloys. Corros Sci 2007;49:1696–701. doi:10.1016/j.corsci.2007.01.001.

[46] Hanawa T. Materials for metallic stents. J Artif Organs 2009;12:73–9. doi:10.1007/s10047-008-0456-x.

[47] Jorcin J-B, Orazem ME, Pébère N, Tribollet B. CPE analysis by local electrochemical impedance spectroscopy. Electrochim Acta 2006;51:1473–9. doi:10.1016/j.electacta.2005.02.128.

[48] Zoltowski P. On the electrical capacitance of interfaces exhibiting constant phase element behaviour 1998:149–54.

[49] Ascencio M, Pekguleryuz M, Omanovic S. An investigation of the corrosion mechanisms of WE43 Mg alloy in a modified simulated body fluid solution : The influence of immersion time 2014;87:489–503.

[50] Roach P, Farrar D, Perry CC. Surface Tailoring for Controlled Protein Adsorption : Effect of Topography at the Nanometer Scale and Chemistry 2006;17:617–21.

[51] Yang Y, Cavin R, Ong JL. Protein adsorption on titanium surfaces and their effect on osteoblast attachment. J Biomed Mater Res A 2003;67:344–9. doi:10.1002/jbm.a.10578.

[52] Materials S, Company AR, Park T. Standard Practice for Assessment of Hemolytic Properties of Materials 1 2009;2002:29–33.

[53] Zhen Z, Liu X, Huang T, Xi T, Zheng Y. Hemolysis and cytotoxicity mechanisms of biodegradable magnesium and its alloys 2015;46:202–6.

[54] Goodman SL. Sheep, pig, and human platelet-material interactions with model cardiovascular biomaterials. J Biomed Mater Res 1999;45:240–50. doi:10.1002/(SICI)1097-4636(19990605)45:3<240::AID-JBM12>3.0.CO;2-C.

[55] Vogler EA, Siedlecki CA. Biomaterials Contact activation of blood-plasma coagulation. Biomaterials 2009;30:1857–69. doi:10.1016/j.biomaterials.2008.12.041.